# Impacts of entrainment on secondary ice production in deep convective clouds

Bowen Z. Portman[1], Paul J. Connolly[1], Alan M. Blyth[2], Rachel L. James[1], and Huihui Wu[1*]
[1]Department of Earth and Environmental Sciences, The University of Manchester, Manchester, UK
[2]National Centre for Atmospheric Science, University of Leeds, Leeds, UK
[*]Now at: Univ Paris Est Créteil and Université Paris Cité, CNRS, LISA, 94010 Créteil, France
**Correspondence:** Paul J. Connolly (paul.connolly@manchester.ac.uk)

**Abstract.**

The accurate representation of secondary ice production (SIP) is essential for describing the microphysics of deep convective clouds, yet the exact mechanisms and efficiencies of SIP are still uncertain. In this study, we used the University of Manchester bin microphysics parcel model to investigate four SIP parameterisations: rime splintering, ice–ice collisional breakup, spherical freezing fragmentation of drops (mode 1), and fragmentation between supercooled droplets and more massive ice particles (mode 2). We simulated air trajectories through deep convective clouds observed during the Deep Convective Microphysics EXperiment (DCMEX) field campaign. Our results show that mode 2, as currently understood and represented in the model, is the key mechanism for explaining the high ice particle concentrations observed. We also present the first systematic study of how different entrainment conditions (~~adiabatic, homogeneous , and inhomogeneous~~ homogeneous and inhomogeneous mixing) affect SIP mechanisms. In our simulations, homogeneous and inhomogeneous mixing with aerosol entrainment provide reasonable agreement with cloud-core and cloud-edge microphysical properties observed during DCMEX, respectively. In addition, the peak liquid water content values in the adiabatic simulations was approximately 300 % of that in the entraining simulations. The entrainment of external aerosols was also found to accelerate the collision–coalescence process under homogeneous mixing, leading to earlier ice enhancement. Our results show that SIP mechanisms, which are dependent on large droplets, such as mode 2, are highly sensitive to different entrainment conditions, emphasising the importance of representing entrainment correctly when including SIP processes in large-scale models.

## 1 Introduction

Ice formation in clouds significantly influences cloud properties and precipitation processes, thereby impacting weather systems and global climate (Planche et al., 2014; Field and Heymsfield, 2015; Tan et al., 2025). However, the formation pathways of ice crystals in clouds remain uncertain, as observed concentrations of ice particles often far exceed what can be explained by primary ice nucleation alone ~~(Hallett et al., 1978; Blyth and Latham, 1993; Crawford et al., 2012; Lasher-Trapp et al., 2021; Lloyd et al., 2024)~~ (Hallett et al., 1978; Blyth and Latham, 1993; Crawford et al., 2012; Ladino et al., 2017; Lasher-Trapp et al., 2021; Lloyd et al., 2024) . Several secondary ice production (SIP) mechanisms have therefore been proposed to explain this discrepancy (Phillips et al., 2018a; Korolev et al., 2020). In our study, we focus on four SIP processes: rime splintering, ice–ice collisions, spherical freezing fragmentation of drops (mode 1), and fragmentation between supercooled droplets and more massive ice particles (mode 2).

Rime-Splintering (RS), also known as the Hallett–Mossop process, is currently the most widely implemented SIP mechanism in cloud microphysics models~~, which occurs~~ . In this process, secondary ice splinters are produced when supercooled droplets collide with and freeze onto riming ice particles. It is active only within a narrow temperature range of -3 to -8 °C (Hallett and Mossop, 1974a) and ~~requires the coexistence of~~ typically occurs when droplets smaller than 12 $\mu$m and larger than 24 $\mu$m in diameter are both present (Mossop, 1978; Harris-Hobbs and Cooper, 1987). However, the large amounts of ice observed in deep convective clouds cannot always be explained by RS, especially in cases where the increase in ice number is too rapid, the temperatures and crystal habits fall outside the RS window, or the necessary conditions for RS are not satisfied (Rangno and Hobbs, 1991; Lawson et al., 2015; Field et al., 2017). ~~Recent experiments~~ The interpretation is further complicated in deep convective clouds, where the role of RS may be difficult to identify because of cloud dynamics. A recent experiment by Seidel et al. (2024) also failed to reproduce the high SIP rates reported in earlier RS studies, thereby questioning the significance of rime splintering under mixed-phase convective conditions. As noted in the review by Korolev et al. (2020), the physical mechanism of RS remains poorly quantified and understood, with the parameterisation still highly uncertain. ~~Therefore, SIP mechanisms that are less constrained by temperature and droplet spectrum conditions, such as Ice–ice collisional breakup and droplet shattering, may be able to explain the observed ice enhancement . However, parametrisations of these other SIP processes are perhaps just as uncertain as for the RS process.~~ Other potential SIP mechanisms therefore need to be considered to better understand ice enhancement in deep convective clouds.

Ice-Ice Collisional Breakup (CB) is the second SIP mechanism investigated in this study. This process refers to the mechanical fragmentation of ice particles during collisions, leading to the formation of new ice crystals. This mechanism has been observed in both aircraft measurements (Schwarzenboeck et al., 2009) and laboratory experiments (Vardiman, 1978; Takahashi and Nagao, 1995; Grzegorczyk et al., 2023). Laboratory studies found that CB is most active near $-16\,^{\circ}\mathrm{C}$ (Takahashi and Nagao, 1995), and field observations also showed substantial secondary ice near $-15\,^{\circ}\mathrm{C}$ (Mignani et al., 2019; Billault-Roux et al., 2023). In simulations of deep convective clouds during the ~~HAIC/HIWC~~High Altitude Ice Crystals and High Ice Water Content (HAIC–HIWC) campaign, Grzegorczyk et al. (2025) found that ~~ice–ice collisional breakup~~ CB was a key contributor to ice enhancement, and that only when combined with ~~rime-splintering~~ RS could the observed high ice crystal concentrations be reproduced. However, the collision efficiency and fragmentation probability of this mechanism remain poorly understood, and future parameterisations will need to be improved accordingly (see the discussion in Korolev et al. 2020).

Finally, we examine ~~the mechanism, and we refer to the spherical freezing fragmentation of drops as according to the description of Phillips et al. (2018a). This mechanism has been identified in both field observations (Lawson et al., 2015) and laboratory experiments (Leisner et al., 2014; Lauber et al., 2018; Keinert et al., 2020). Many studies have incorporated as a droplet fragmentation process in model simulations (Sotiropoulou et al., 2020; Huang et al., 2017; Grzegorczyk et al., 2025) . However, James et al. (2023) found that its contribution was relatively minor in their simulations of an idealised shallow convective cloud.~~

~~We refer to the~~ fragmentation of freezing drops, also known as drop shattering (DS), in which supercooled droplets fragment during freezing and produce secondary ice particles. To better characterise these processes, Phillips et al. (2018b) described DS as comprising two modes, with mode 1 (M1) representing fragmentation during the spherical freezing of droplets, and mode 2 (M2) representing fragmentation during collisions between supercooled droplets and more massive ice particles~~as . To date, only one laboratory study has directly examined~~. According to Phillips et al. (2018b), fragment numbers in M1 depend strongly on both temperature and droplet size, exhibiting a pronounced thermal peak near -15 °C and increasing with droplet size. In contrast, M2 ~~(James et al., 2021), and its parameterisation still requires substantial testing. Nevertheless, many studies have already incorporated into their investigations of SIP (Phillips et al., 2018a; Sotiropoulou et al., 2020; Zhao and Liu, 2022; James et al., 2023), and James et al. (2023) suggested that might be a key SIP mechanism in convective clouds where large droplets are present.~~

shows no clear evidence of a thermal peak and instead increases with dimensionless collision energy and supercooling, requiring the presence of large supercooled droplets and more massive ice particles. DS has increasingly been incorporated into numerical studies of SIP in recent years, reflecting that it may represent an important source of secondary ice. For example, James et al. (2023) investigated M2 within the framework of Phillips et al. (2018b) in parcel model simulations of idealised shallow convective clouds, and compared it with RS, M1, and CB. Their results suggest that, under conditions where RS is limited, M2 may represent an important source of secondary ice in shallow convective clouds, whereas the contribution from M1 is relatively small. In this study, we ~~aim to use the University of Manchester bin-microphysics parcel model (BMM, based on an updated version of the framework developed by James et al. 2023 and Fowler et al. 2020) to investigate secondary ice production in the~~ follow the framework of Phillips et al. (2018b) and James et al. (2023) and examine DS by separately analysing M1 and M2, given their distinct physical characteristics.

Many SIP mechanisms (e.g. RS, M1, and M2) are highly sensitive to warm-phase microphysical conditions in clouds, particularly liquid water content and droplet size distributions. Previous studies have shown that these properties can be strongly affected by entrainment in deep convective clouds, particularly by how entrained environmental air mixes with cloudy air (Morrison et al., 2022b; Chandrakar et al., 2021b). Homogeneous and inhomogeneous mixing are commonly regarded as two idealised limiting regimes of entrainment-mixing in clouds (Baker et al., 1980; Lehmann et al., 2009). Homogeneous mixing assumes that entrained air first mixes thoroughly with cloud air, after which the droplet population experiences an approximately uniform reduction in relative humidity, whereas in inhomogeneous mixing the mixing is incomplete and different droplets may be exposed to different local humidity conditions. Yeom et al. (2017) found that the microphysical relationships in most cloud segments of continental stratocumulus were more consistent with homogeneous mixing. However, other observational studies have suggested that homogeneous and inhomogeneous mixing can both occur in real clouds, depending on cloud region, environmental conditions, and cloud life cycle stage. For example, Lehmann et al. (2009) showed that homogeneous mixing was more likely near the cloud core, whereas inhomogeneous mixing tended to dominate in more diluted cloud regions.

Modelling studies of SIP in deep convective clouds ~~observed during the campaignover New Mexico (Finney et al., 2024), and to explore the potential influence of different entrainment representations on SIP. The DCMEX field~~ have often reported contrasting conclusions regarding the dominant mechanisms. This may be because the relative importance of SIP processes can vary substantially over the cloud lifecycle. For example, Huang et al. (2022) found that DS dominated during the early stage of convection, whereas CB became more important at later stages, using the bulk P3 scheme in Weather Research and Forecasting (WRF). This variation in the dominant SIP mechanisms occurs even in studies based on the same observational case from the HAIC–HIWC campaign. For example, Qu et al. (2022) used a bulk microphysics scheme and suggested that DS was the dominant SIP mechanism during a later stage of their simulation (90 to 150 min). In contrast, Grzegorczyk et al. (2025) used a 3D bin microphysics model and found that RS and CB were more important, with DS having only a limited effect at the mature stage of the simulated cloud. This discrepancy may be explained by differences in how warm microphysical processes and entrainment are represented across models, thereby affecting simulated SIP. In many commonly used microphysics schemes, especially those employing simplified bulk representations, entrainment is often treated as homogeneous mixing (Xu et al., 2021). However, mixing can also be inhomogeneous in deep convective clouds because of their complex structure and strong spatial variability. It is therefore necessary to systematically examine how different representations of entrainment affect SIP.

## 2 DCMEX

The Deep Convective Microphysics EXperiment (DCMEX) campaign was conducted in July and August 2022 over the Magdalena Mountains ~~, where conditions~~ near Socorro, New Mexico, with the aim of characterising the microphysics and dynamics of deep convective cloud formation, including improved understanding of SIP mechanisms (Finney et al., 2024). Conditions in this region are highly favourable for the development of multiple-thermal cumulus congestus~~convection limited~~. These clouds are typically confined to the mountain range ~~that transitions to~~ and can transition into deeper thunderstorms (Finney et al., 2024). The occurrence of theseclouds is strongly influenced by the North American Monsoon (NAM), ~~when~~ during which moist inflows from the Gulf of Mexico and the eastern Pacific ~~occur~~ prevail between June and September (Adams and Comrie, 1997; Erfani and Mitchell, 2014).

A number of studies have investigated cloud processes during the DCMEX campaign. Among these, Wu et al. (2025b) conducted a combined modelling and observational analysis of warm cloud processes in two DCMEX cases and ~~also~~ found that aerosol entrainment plays a key role in broadening the droplet size distribution (DSD), which ~~is expected to be crucial~~ has important implications for subsequent investigations of the ice phase in clouds. Previous work at the same site by Blyth and Latham (1993) suggested that RS was ~~likely~~ responsible for the high ice crystal concentrations observed in these clouds. The contributions and relative importance of different SIP mechanisms in deep convective clouds in this region remain to be systematically assessed.

Section 2.1 describes the measurements used in this study, including the key instrumentation, while Section 2.2 introduces the case studies analysed in this work.

~~In previous modelling studies of deep convective clouds, conflicting conclusions have been reached regarding the dominant SIP mechanisms. While some studies suggest that DS provides the primary contribution~~

~~(Qu et al., 2020; Huang et al., 2022; James et al., 2023), others attribute it to CB and RS (Grzegorczyk et al., 2025). Even for simulations of the same observational case, different modelling studies have produced conflicting estimates of how SIP mechanisms affect ice concentrations (Qu et al., 2022; Grzegorczyk et al., 2025). Differences in the representation of warm-rain processes across models may have potential impacts on the simulated SIP. Variations in how collision–coalescence efficiency, raindrop growth by accretion, and CCN activation are treated can all affect droplet sizes, while different entrainment parameterisations can influence the broadening of droplet distribution. These factors are particularly critical for SIP mechanisms such as RS and M2 that dependent on the presence of large droplets.~~

~~The structure of this paper is as follows. Section 2 introduces the DCMEX campaign and the case study. Section 3 describes the BMM configuration and the entrainment representation. Section 4 presents the results and the sensitivity analyses, followed by the discussion in Section 5 and the conclusions in Section 6.~~

## 3 ~~DCMEX~~

### 2.1 Measurements

~~The campaign was conducted in July and August 2022 over the Magdalena Mountains near Socorro, New Mexico, aimed to characterise the microphysics and dynamics of deep convective cloud formation, with one of its main challenges to better understand the secondary ice production mechanisms (Finney et al., 2024).~~

A key component of DCMEX was the Facility for Airborne Atmospheric Measurements (FAAM) British Aerospace Engineering-146 (~~BAE-146~~BAe-146) aircraft, which was equipped with a comprehensive suite of aerosol and cloud microphysics instruments. During the DCMEX flights, the aircraft ~~typically~~ followed a kite-shaped pattern around the Magdalena Mountains for the INP and aerosol sampling parts of the flight, while straight and level passes were made through the clouds during cloud sampling. The right panel of Fig. 1 shows the flight track for Flight C300 on 22 July 2022, which is representative of the other flights that followed a similar plan view. All flights followed a similar pattern, starting with low-level aerosol runs to characterise the boundary-layer inflow, followed by cloud passes through developing convection to investigate microphysical properties within the mixed-phase region. In addition, dropsondes were released near the Magdalena Mountains to obtain vertical profiles of thermodynamic and wind fields (Finney et al., 2024). Below, we briefly summarise the instruments used in this study.

The Aerosol Mass Spectrometer (AMS) and the Scanning Mobility Particle Sizer (SMPS) were used to measure the composition and size distribution of sub-micron aerosol. The AMS provided estimates of the effective hygroscopicity parameter ($\kappa$) of the aerosol, which were used to derive their Cloud Condensation Nuclei (CCN) properties for input into the Bin Microphysics Model (BMM). The SMPS was employed to characterise the aerosol size distribution near the cloud base, as shown in Wu et al. (2025b).

The ~~DMT~~ cloud droplet probe (CDP-2) was used to measure ~~(~~the droplet size distribution (DSD) over the size range 2 ~~–~~to 50~~$\mu$m)~~ $\mu$m and to derive ~~(Lance et al., 2010b), whereas was~~ cloud droplet number concentration (CDNC) (Lance et al., 2010b). The relative dispersion of the DSD was also calculated as the ratio of the standard deviation of droplet diameter to the

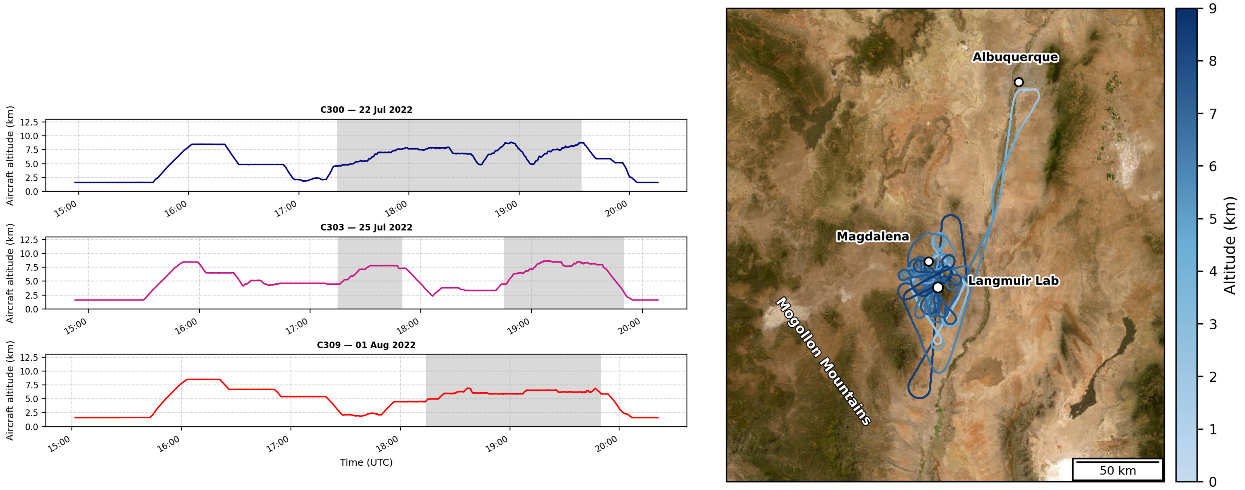

**Figure 1.** The left panel shows the time series of aircraft altitude for the three selected DCMEX cases, with shaded periods indicating cloud penetration. The right panel shows the corresponding flight track for the case on 22 July 2022 (C300).

mean droplet diameter. Liquid water content (LWC) was obtained from a Nevzorov hot-wire probe following the Met Office processing method (Korolev et al., 1998; Abel et al., 2014).

The Cloud Particle Imager (CPI, version 2.5~~; SPEC Inc.~~) was used to obtain high-resolution images of cloud particles larger than 8 $\mu$m and to derive ice particle concentration. Although the CPI has a relatively small sample volume compared with the 2D-S, data from multiple flight segments were averaged to make the results more reliable and representative. The high-resolution imagery was also used to identify potential SIP mechanisms in this study (Korolev and Leisner, 2020; Korolev et al., 2022); further discussion is provided in Section. 4.3.

## 2.2 Case Study

The data used in this study were collected from 19 July to 7 August 2022 (flight C298–C314). In the early phase of the campaign, from 19 to 22 July (Flight C298–C300), the airmass originated from north-western (NW) flow from the Pacific over the continent towards the Magdalena Mountains, resulting in relatively lower cloud-base temperatures ($T_{\mathrm{cb}} \approx 1.5^{\circ}\mathrm{C}$) and lower humidity compared to later in the campaign. Around 24 July, a shift to south-eastern (SE) flow from the Gulf of Mexico introduced warmer and moister conditions, marking a transition observed in the subsequent flights (Flights C302–C314). After 28 July, the clouds generally maintained relatively high cloud-base temperatures ($T_{\mathrm{cb}} \approx 5.67^{\circ}\mathrm{C}$) and relative humidity.

In this study, ~~we focus on three~~ 15 flight cases were simulated, as listed in Table 1. Three representative cases, 22 July (C300), 25 July (C303), and 01 August (C309), ~~which were selected~~ are selected for detailed analysis based on the evolution of the airmass characteristics described above. The flight altitude for the three cases is shown in the left panel of Fig. 1. The 22 July case was chosen as it represents typical convective clouds that developed under the NW flow during the early phase of the campaign, while the 25 July case represents the early stage of SE inflow.

The 01 August case represents the later phase with SE flow. It was selected because the cloud was in a relatively early stage of development, before the convection had penetrated the detrainment layer. The in-situ sounding revealed a pronounced temperature inversion at around 7 km. However, the observed cloud top reached approximately 14.4 km (Finney et al., 2024), suggesting that the convection was strong enough to break through the inversion and later developed up to the tropopause. Such inversion-breaking convection is commonly observed over the mountainous southwest United States during the summer monsoon (Adams and Souza, 2009; Fonseca-Hernandez et al., 2021).

## 3 Bin microphysics parcel model

### 3.1 Model description

The model used in this study is the University of Manchester BMM, based on an updated version of the framework developed in previous studies (Topping et al., 2013; Fowler et al., 2020; James et al., 2023), with the source code available at https://github.com/UoM-maul1609/bin-microphysics-model. ~~In the model, aerosols, cloud droplets and ice particles are represented on bin grids. The input aerosol size distribution for each external mixture $j$ is expressed~~ A simplified schematic overview of the main BMM framework is shown on the left side of Fig. 2.

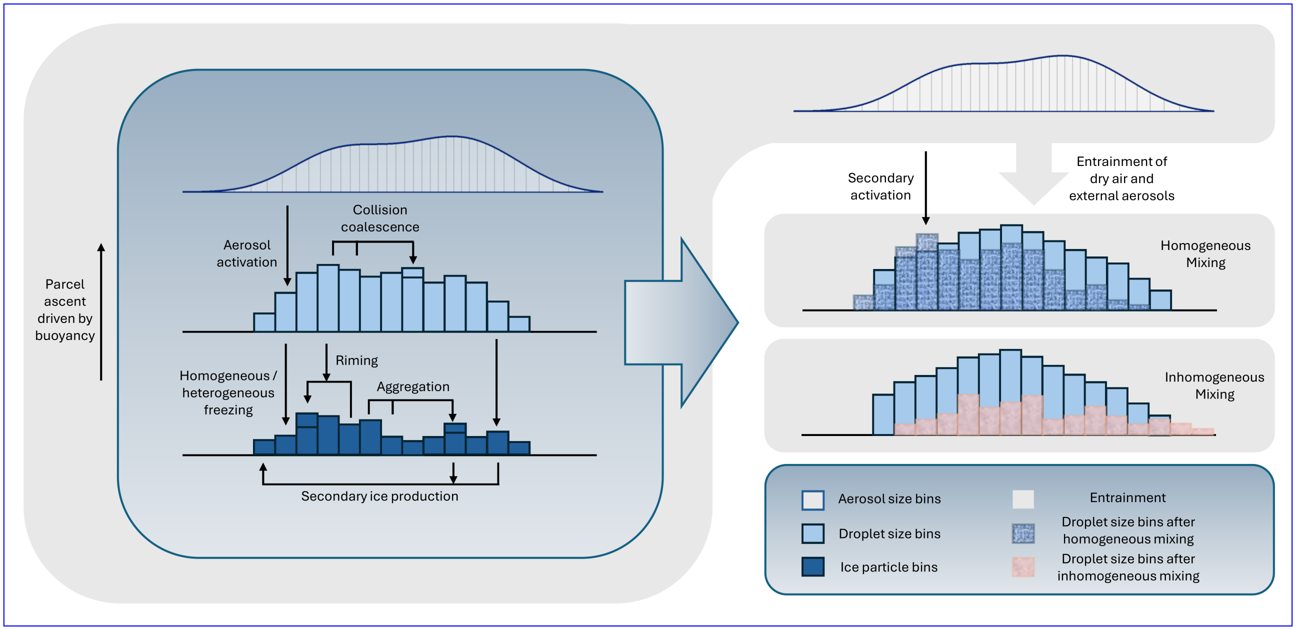

**Figure 2.** Schematic representation of the BMM parcel model. The left-hand side shows the main model framework, including the key microphysical processes and representations of the aerosol, droplet, and ice particle size bins from top to bottom. The right-hand side illustrates the two entrainment-mixing representations in the BMM, homogeneous mixing and inhomogeneous mixing.

In the BMM, particles are represented by two particle size distributions, droplet size bins and ice particle bins, each comprising 80 bins. Both distributions additionally include 60 aerosol bins (10 nm to 3 $\mu$m). The aerosol bins are not defined using linear or logarithmic spacing in particle size. Instead, the bin edges are defined from the initial aerosol number concentration so that each bin contains approximately equal particle numbers. This approach is intended to reduce discretisation artefacts during aerosol activation, thereby avoiding step-like increases in activated particle number concentration in response to changes in updraft or supersaturation.

The aerosol population can be represented by one or more externally mixed components with different chemical compositions. For each externally mixed component, particles are assumed to be internally mixed across the size distribution, so that their chemical composition does not vary with particle size. In this study, only a single externally mixed component is considered. Its initial size distribution is represented as the sum of ~~$M$ lognormal modes. The lognormal size distribution for each mode $j$ is given by Equation 1.~~ multiple lognormal modes, as follows:

$$\left[\frac{dN}{d\ln D}\right]_j = \sum_i^M \frac{N_{ap,i,j}}{\sqrt{2\pi}\ln\sigma_{g,i,j}} \exp\left(-\frac{\ln^2(D/d_{m,i,j})}{2\ln^2\sigma_{g,i,j}}\right) \tag{1}$$

where ~~$\left[\frac{dN}{d\ln D}\right]_j$~~ $\left[\frac{dN}{d\ln D}\right]_j$ is the aerosol number size distribution (cm~~$^{-3}$) for the external mixture $j$, $D$~~$^{-3}$) for external mixture $j$, $D$ is the particle diameter (m), ~~$N_{ap,i,j}$~~ $N_{ap,i,j}$ is the total aerosol number concentration (cm~~$^{-3}$~~$^{-3}$) of mode ~~$i$ within mixture $j$, $d_{m,i,j}$~~ $i$ within external mixture $j$, $d_{m,i,j}$ is the geometric mean diameter (m), and ~~$\sigma_{g,i,j}$~~ $\sigma_{g,i,j}$ is the geometric standard deviation ~~describing the width~~ of the lognormal ~~distribution. The summation over $M$ modes allows representation of multi-modal aerosol populations (e.g. Aitken, accumulation and coarse modes) within each external mixture.~~

~~The model allows for several initial external mixtures of different composition, with aerosol composition represented by specifying a $\kappa$ value for each mode$j$~~mode. In this study, $j = 1$ because only a single externally mixed ~~aerosol type is considered($j = 1$), representing ammonium sulfate, consisting of~~ component is considered, and $M = 2$ denotes the two lognormal modes ~~($M = 2$) with a uniform hygroscopicity parameter ($\kappa$) across the size distribution~~used to represent the initial aerosol size distribution: the Aitken and accumulation modes.

The ~~aerosol size distribution is discretised into bins with the lowest bin edge set at 10 nm. The initial water mass associated with this bin is determined by solving for the zero of the Köhler equation. Each subsequent bin increases in water mass~~ hygroscopic growth of aerosol particles is described using $\kappa$-Köhler theory, in which particle hygroscopicity is represented by the parameter $\kappa$ (Petters and Kreidenweis, 2007). In this study, $\kappa$ is assumed to remain constant across all size bins. The initial wet diameter and corresponding liquid water mass of aerosol particles are determined by assuming equilibrium with the prescribed environmental relative humidity, based on $\kappa$-Köhler theory. This initial wet state is represented numerically on a mass-based bin structure, with the mass of adjacent bins increasing by a factor of $2^{1/2}$~~, resulting in a total of 140 bins. For each bin, the aerosol mass is calculated numerically using a root-finding algorithm to ensure consistency between the specified hygroscopicity parameter $\kappa$ and the assigned water mass. The number concentration in each bin is then obtained by mapping Equation 1 onto the bin grid~~.

~~Condensation and evaporation processes are calculated using the solver from NETLIB library (Brown et al., 1989), which is well suited to handle the stiff nature of~~ The warm microphysical processes considered in this study include diffusional droplet growth and collision–coalescence of liquid particles. Diffusional growth rates account for kinetic effects and corrected diffusivity and thermal conductivity terms (Jacobson, 2005; Pruppacher et al., 1998), whereas collision–coalescence is described by the stochastic collection equation and solved using the method of Bott (1998). In addition, the model also includes entrainment of dry air and external aerosol, as described in Sect. 3.2.

The cold microphysical processes considered in this study include homogeneous and heterogeneous freezing, vapour depositional growth of ice particles, ice–ice aggregation, riming, and secondary ice production. Homogeneous freezing of supercooled droplets is represented following the formulation of Koop et al. (2000). Heterogeneous freezing in this study is represented using the parameterisation of Daily et al. (2025), a recently developed formulation constrained by observations from the DCMEX campaign. To assess the sensitivity of the results to the ~~associated differential equations.This approach ensures numerical stability and accuracy in representing droplet growth and evaporation across the bin grid~~representation of ice-nucleating particles, DeMott et al. (2010) is also included for comparison. The differences between the two parameterisations are discussed in Sect. 4.3, with additional details provided in Sect. S2 of the Supplement.

~~For the ice phase, several additional prognostic variables~~ In the BMM, ice particles are represented by a separate set of bins from liquid particles. Additional prognostic properties are tracked in each ~~bin. These include the crystal aspect ratio($\Phi$), the rime mass($\varrho$),~~ ice bin, including the aspect ratio, particle volume, rime mass, and the number of ice crystal monomers per ice particle~~($N_{mon}$), and the crystal density ($\rho_{crystal}$). It is further assumed that any rime mass freezes instantaneously upon accretion.~~

~~Collision–coalescence of cloud droplets, coagulation of aerosols, inertial impaction of aerosols, ice particle aggregation, and riming are~~. Riming and ice–ice aggregation are also represented by numerically solving the stochastic collection equation (SCE) using the exponential flux method of Bott (1998)~~, with collision kernels from Jacobson (1999). During these collection processes, properties such as the total aerosol mass in colliding bins, as well as the ice-phase variables ($\Phi$, $\varrho$, $N_{mon}$, and $\rho_{crystal}$), are consistently conserved during the collection processes.~~. A more detailed description of the ice particle bin representation is provided by James et al. (2023). The parameterisation of SIP is described in Sect. S1.

### 3.2 Entrainment Representation

~~Two main approaches are consideredto represent the entrainment process~~In this study, two types of entrainment processes are considered: homogeneous and inhomogeneous mixing. In the ~~BMM~~model, homogeneous mixing is ~~assumed, where environmental air continuously mixes with~~ represented by continuously incorporating environmental air into the parcel and ~~is assumed to instantaneously dilute~~ instantaneously mixing it at each time step~~. The resulting decrease in humidity reduces the growth rate of droplets of all sizes, and smaller droplets evaporate more rapidly as the relative humidity decreases, causing a shift of the droplet size distribution towards smaller diameters~~, leading to a dilution of the parcel thermodynamic properties. This is implemented by including additional equations in the solver routine~~that are passed to~~, which are integrated using the variable-coefficient ordinary differential equation (VODE) solver. The theory is described in Pruppacher and Klett (1997, chapter 12). ~~The entrainment rate for a jet $J$ is defined as~~

In this model, the parcel is represented as a jet, allowing entrainment to occur through the front interface of the plume. The evolution of the vertical velocity ($W$), parcel radius ($R_j$), and water vapour mixing ratio ($q_v$) is explicitly represented, and the entrainment of ambient aerosol is also included. The entrainment rate ($\mu_J$) for the jet parcel is therefore defined as

$$\mu_J = \frac{1}{F_m}\frac{dF_m}{dz} = \frac{C_J}{R_J} \tag{2}$$

where ~~$F_m$~~ $F_m = \pi R_J^2 \rho W$ is the total mass flux of the rising parcel (kg ~~$\mathrm{m^{-2}\,s^{-1}}$), $C_J \approx 0.2$ is the~~ $\mathrm{s^{-1}}$), $\rho$ is the parcel density, $C_J$ is the entrainment parameter, set to 0.2 based on previous laboratory studies, and $R_J$ is the ~~radius of the jet . The ascent of the parcel is calculated by considering the buoyancy and reaction of the surrounding air (see Equation 12.25 of Pruppacher and Klett, 1997)~~jet radius, which is set to 1000 m in this model.

The ~~time~~ evolution of the parcel's vertical velocity $W$ ($\mathrm{m\,s^{-1}}$) is described by

$$\frac{dW}{dt} = \frac{g}{1+\gamma}\left(\frac{T-T'}{T'} - w_L\right) - \frac{\mu}{1+\gamma}\frac{\mu_J}{1+\gamma}W^2 \tag{3}$$

where $g$ is the gravitational acceleration (9.81 $\mathrm{m\,s^{-2}}$), $\gamma \approx 0.5$ is the moisture correction parameter accounting for the virtual effect of water vapour, $T$ and $T'$ are the temperatures of the parcel and the environment (K), respectively, ~~$w_L$ is the fractional mass of condensed liquid water relative to the total moist air, following Pruppacher and Klett (1997), and $\mu$ is the entrainment rate ($\mathrm{m^{-1}}$), which accounts for momentum loss due to mixing with environmental air~~$w_L$ is the liquid water mixing ratio ($\mathrm{kg\,kg^{-1}}$).

The ~~radius~~ evolution of the jet ~~changes during ascent according to~~ radius is given by

$$\frac{dR_J}{dt} = \frac{R_J}{2}\left(\mu_J W - \frac{1}{\rho}\frac{d\rho}{dt} - \frac{1}{W}\frac{dW}{dt}\right) \tag{4}$$

~~where $R_J$ is the jet mass flux of the rising parcel ($\mathrm{kg\,m^{-2}\,s^{-1}}$); $t$ is time (s); $\mu_J$ is the entrainment rate ($\mathrm{m^{-1}}$); $W$ is the parcel vertical velocity ($\mathrm{m\,s^{-1}}$); $\rho$ is air density ($\mathrm{kg\,m^{-3}}$); $d\rho/dt$ is the material rate of change of density ($\mathrm{kg\,m^{-3}\,s^{-1}}$); and $dW/dt$ is the vertical acceleration ($\mathrm{m\,s^{-2}}$)~~All variables are as defined above.

Finally, the water vapour mixing ratio is calculated by a statement of conservation of water substance

$$\frac{dw_v}{dt} = -\frac{dw_L}{dt} - \frac{dw_i}{dt} - \mu_J\left(w_v - w_v' + w_L + w_i\right) \tag{5}$$

where $w_v$ is the water-vapour mixing ratio within the parcel ($\mathrm{kg\,kg^{-1}}$); ~~$w_L$ is the liquid-water mixing ratio ($\mathrm{kg\,kg^{-1}}$);~~ $w_i$ is the ice-water mixing ratio ($\mathrm{kg\,kg^{-1}}$); ~~$t$ is time (s); $\mu_J$ is the entrainment rate ($\mathrm{m^{-1}}$);~~ and $w_v'$ is the water-vapour mixing ratio of the entrained environmental air ($\mathrm{kg\,kg^{-1}}$).

The BMM also allows entrainment to be represented as inhomogeneous mixing (Baker et al., 1980), in which environmental air is ~~introduced~~ not instantaneously and uniformly mixed with the parcel air, but is instead entrained intermittently into the parcel ~~as discrete packetsrather than being instantaneously mixed~~in the form of discrete packets. The same mean entrainment rate as in the homogeneous case is applied~~, but mixing is implemented outside~~ . However, unlike the homogeneous mixing representation, the mixing process is not solved continuously within the VODE solver~~using~~ , but is instead implemented as discrete events over a longer 10~~,~~ s timestep to represent intermittent entrainment. ~~This formulation assumes that the mixing timescale is less than the evaporation timescale. Under this inhomogeneous mixingregime, small droplets in the entrained regions may completely evaporate while larger ones remain nearly unchanged. As a result, the total droplet number concentration becomes smaller than in~~ For inhomogeneous mixing, the ~~homogeneous case, producing greater supersaturation and enhanced condensational growth of the remaining droplets. Since the larger droplets are less affected by evaporation, collision–coalescence proceeds more efficiently, further accelerating droplet growth. A~~ droplet number concentrations in each size bin are adjusted to conserve parcel humidity, thereby preventing a uniform reduction in droplet size across the entire spectrum as occurs in homogeneous mixing. When inhomogeneous mixing causes droplet evaporation, the released aerosol particles are returned to the discrete packets of subsaturated air within the parcel, where they may become re-activated later. A simplified schematic of the two entrainment ~~configurations is shown in~~ representations in the BMM is shown on the right of Fig. 2.

~~Schematic representation of the parcel model with a simplified entrainment–mixing framework, illustrating its influence on the droplet size distribution (DSD). The top panel shows the adiabatic case, without entrainment. The middle panel shows homogeneous mixing, where dry air and aerosols are uniformly mixed into the parcel. The bottom panel shows inhomogeneous mixing, in which environmental air is entrained as discrete packets. Adapted from (Lu et al., 2023).~~

### 3.3 ~~Secondary ice parameterisations~~

~~The parameterisations of the four SIP mechanisms implemented in the BMM are based on the formulations of James et al. (2023). Rime splintering () is parameterised following Reisner et al. (1998), which is based on the laboratory experiments of Hallett and Mossop (1974b). Splinter production is linked to the riming rate, which in the model is parameterised as the accretion of cloud droplets by graupel, considering the collection efficiency, relative fall velocity, and liquid water content. The process is active for $-7.5 \leq T \leq -2.5\,^{\circ}$C, with maximum efficiency near $-5\,^{\circ}$C.~~

~~Collisional breakup () is parameterised following Phillips et al. (2017). The scheme relates fragment production to the collisional kinetic energy between ice particles, with efficiency modulated by ice particle type, density, riming, and aspect ratio. It accounts for collisions between graupel or hail, hail with hail, and snow or dendritic crystals with other ice particles.~~

~~Freezing fragmentation of drops is represented by two parameterisations from Phillips et al. (2018a). Mode 1 () describes the shattering of supercooled raindrops into multiple fragments upon freezing, with two size regimes distinguished: numerous small fragments and fewer large fragments, and is most efficient around $-15\,^{\circ}$C. Mode 2 () represents the fragmentation of supercooled drops upon collision with ice particles, controlled by the ratio of collisional kinetic energy to surface energy.~~

~~Fragmentation occurs when drop diameters exceed 0.15 mm and the drop mass is smaller than that of the colliding ice particle, with the number of fragments depending on the collision energy.~~

### 3.3 Initial conditions

In our study, simulations are initialised at cloud base with an initial relative humidity of 0.95. All simulations are run for about 2.2 hours (8000s) with a timestep of 10 s, and the parcel radius is set to 1000 m. The initial aerosol size distribution is represented by a two-mode lognormal fit derived from SMPS observations (see Fig. S1 and Table. S1). Table 1 summarises the initial aerosol and cloud-base conditions used to initialise the simulations, including the cloud-base pressure ($P_{\mathrm{cb}}$), aerosol density ($\rho$), and ~~hygroscopicity parameter ($\kappa$)~~.

**Table 1.** Cloud-base thermodynamic and aerosol properties for the simulated cases, including the lifting condensation level (LCL), cloud-base temperature ($T_{\mathrm{cb}}$), temperature perturbation ($\Delta T$), cloud-base pressure ($P_{\mathrm{cb}}$), updraught velocity ($w_{\mathrm{cb}}$), aerosol density ($\rho$), and hygroscopicity parameter ($\kappa$).

| Date | Flight | LCL (km) | $T_{\mathrm{cb}}$ (°C) | $\Delta T$ (K) | $P_{\mathrm{cb}}$ (hPa) | $w_{\mathrm{cb}}$ (m s$^{-1}$) | $\rho$ (kg m$^{-3}$) | $\kappa$ |
|---|---|---|---|---|---|---|---|---|
| Tue 19 Jul | C298 | 5.12 | 0.27 | 2.5 | 562.04 | 2.5 | 1566.84$^*$ | 0.3811$^*$ |
| Wed 20 Jul | C299 | 4.99 | 1.47 | 0.2 | 571.23 | 1.0 | 1566.84 | 0.3811 |
| Fri 22 Jul | C300 | 4.86 | 2.68 | 1.0 | 579.20 | 2.5 | 1484.95 | 0.2674 |
| Sun 24 Jul | C302 | 4.10 | 5.44 | 1.0 | 635.06 | 2.5 | 1606.81 | 0.4149 |
| Mon 25 Jul | C303 | 3.95 | 7.62 | 2.0 | 646.06 | 2.5 | 1617.27 | 0.4069 |
| Tue 26 Jul | C304 | 3.92 | 7.06 | 2.0 | 648.35 | 1.0 | 1637.87 | 0.4461 |
| Wed 27 Jul | C305 | 4.07 | 6.60 | 1.0 | 636.82 | 2.5 | 1650.06 | 0.4662 |
| Fri 29 Jul | C306 | 4.06 | 5.98 | 2.5 | 636.90 | 2.5 | 1603.63 | 0.3939 |
| Sat 30 Jul | C307 | 3.84 | 7.38 | 0.5 | 656.25 | 1.5 | 1571.12 | 0.4006 |
| Sun 31 Jul | C308 | 4.39 | 2.77 | 2.0 | 613.79 | 2.5 | 1569.68 | 0.3824 |
| Mon 1 Aug | C309 | 4.22 | 5.26 | 1.5 | 627.72 | 2.5 | 1547.22$^*$ | 0.3482$^*$ |
| Tue 2 Aug | C310 | 4.29 | 4.97 | 1.0 | 621.02 | 1.0 | 1547.22 | 0.3482 |
| Thu 4 Aug | C312 | 4.37 | 4.62 | 1.5 | 614.25 | 1.5 | 1591.61$^*$ | 0.3921$^*$ |
| Sat 6 Aug | C313 | 4.31 | 5.16 | 1.0 | 619.58 | 1.0 | 1591.61 | 0.3921 |
| Sun 7 Aug | C314 | 4.39 | 2.76 | 2.0 | 613.65 | 2.5 | 1541.35 | 0.3650 |

Values marked with an asterisk ($^*$) were taken from ~~a neighbouring~~ the closest available DCMEX case with similar atmospheric conditions because ~~no data were~~ case-specific data were not available.

Seven simulations were performed for each case to represent the seven mixing scenarios considered in this study (see Table 2). These scenarios include two primary types of mixing, homogeneous (HOM) and inhomogeneous (INHOM), each examined with or without entrained aerosol (EA). For the inhomogeneous scenarios, we further distinguished whether the entrained aerosol particles were released (RA) following the mixing process. In addition, a fully adiabatic reference case (ADIA) was included.

In the BMM, the initial parcel temperature was set to the potential temperature with an added perturbation ($\Delta T$). The value of $\Delta T$ and the initial updraught velocity at cloud base ($w_{\mathrm{cb}}$) were both adjusted until the simulated liquid water content (LWC) agreed with the upper boundary of the observed profiles, which aimed to model the cloud core where liquid water contents are typically high (Lehmann et al., 2009). For the adiabatic simulations, the ascent rate was constrained to match that in the non-adiabatic simulations, and the parcel was stopped at the same model cloud top. The entrainment parameter was set to 0 for the adiabatic simulations, while 0.2 was used for all non-adiabatic cases.

**Table 2.** Summary of the mixing scenarios considered in this study. HOM: homogeneous mixing; INHOM: inhomogeneous mixing; EA: entrained aerosol; RA: released aerosol; ADIA: adiabatic case.

| Scenario | Mixing type | Entrain aerosol | Release aerosol |
|---|---|---|---|
| HOM+EA | Homogeneous | Yes | – |
| HOM | Homogeneous | No | – |
| INHOM+EA+RA | Inhomogeneous | Yes | Yes |
| INHOM+RA | Inhomogeneous | No | Yes |
| INHOM+EA | Inhomogeneous | Yes | No |
| INHOM | Inhomogeneous | No | No |
| ADIA | Adiabatic | – | – |

For each sensitivity experiment, the SIP mechanisms (RS, CB, M1, and M2) were investigated individually, as well as in simulations with all mechanisms switched off and with all mechanisms activated. We also performed sensitivity tests with the heterogeneous freezing parameterisations of ~~?~~ Daily et al. (2025) and DeMott et al. (2010), given that SIP processes depend on the availability of primary ice crystals.

## 4 Results

We used the BMM to simulate the trajectories of individual air parcels for all 15 cases from the DCMEX campaign. Each parcel was initialised at the model cloud base and triggered by a thermal perturbation. Once the parcel reached buoyancy equilibrium, it remained at that level, while the internal microphysical processes and associated calculations continued throughout the simulation. Figures ~~S2–S4~~ S3–S5 present the vertical profiles of ~~CDNC, LWC, and~~ cloud droplet number concentration (CDNC), liquid water content (LWC), and effective diameter ($D_{\mathrm{eff}}$) for all simulated cases. Figure ~~S5~~ S9 shows the total ice crystal number concentration in the control simulation, where all SIP mechanisms were switched off and only primary ice from INP activation was considered, based on DCMEX INP measurements ~~(?)~~(Daily et al., 2025). Figures ~~S6–S10 present~~

~~the ice enhancement (i.e. the difference between the SIP ice crystal number concentration and control ice crystal number concentration), including~~ S10–S14 show the simulated ice enhancement for all 15 cases, for simulations in which each SIP mechanism (RS, CB, M1, M2) is activated individually ~~, as well as the configuration with all mechanisms activated together~~and for the simulation in which all mechanisms are activated simultaneously.

This section is organised into four parts. Section 4.1 presents the modelled evolution of liquid-phase properties (CDNC, LWC, and $D_{\mathrm{eff}}$) for the three selected cases, and Section 4.2 shows the impact of entrainment on the droplet size distribution (DSD), including the vertical evolution of dispersion within the cloud. Section 4.3 compares observed and simulated clouds with all SIP mechanisms activated, and Section 4.4 analyses ~~the contributions of~~ how individual SIP mechanisms contribute to ice enhancement.

### 4.1 Bulk Liquid-Phase Cloud Properties

To quantify the ~~contribution of SIP~~ effect of SIP on ice enhancement within the parcel, we first need to examine the liquid phase, including the vertical profiles of liquid water content (LWC), cloud droplet number concentration (CDNC), and $D_{\mathrm{eff}}$ from both observations and simulations under seven different mixing assumptions. The left panel of Figure 3 presents the evolution of LWC for the three selected cases, showing only small differences ~~between the entrainment types because our~~ among the non-adiabatic simulations because the parcel model entrains the same total mass of environmental air ~~for both HOM and INHOM simulations. The~~ in each case. These simulations closely reproduce the ~~maximum values of the observations, reaching peak values~~ observed peak LWC values, with maxima of approximately 1.0, 1.25, and 1.25 g m$^{-3}$ for the 22 July, 25 July, and 1 August cases, respectively, near the parcel ~~model~~ maximum height. As expected, the observed values of LWC are much less than the adiabatic values due mainly to entrainment, while the ADIA simulations produce significantly higher LWC near the model cloud top, reaching approximately 300% of those in the HOM and INHOM simulations.

It also should be noted that the CDP data collected during the DCMEX campaign represent instantaneous cloud measurements along the flight tracks, and the histories of the sampled cloud parcels cannot be determined. Therefore, the CDNC (middle-left panel), $D_{\mathrm{eff}}$ (middle-right panel), and dispersion (right panel) distributions of Figure 3 are interpreted in terms of LWC to identify cloud-core (yellow) and cloud-edge (blue) regions for each case. Following the findings of Lehmann et al. (2009), cloud-core regions are characterised by high liquid water content, as well as droplet concentrations and droplet size distributions that are broadly consistent with homogeneous mixing, whereas cloud-edge regions experience stronger evaporation, lower LWC, and are characterised by inhomogeneous mixing.

~~For the adiabatic simulations (ADIA )~~The evolution of CDNC within the parcel is shown in the middle-left panel of Figure 3. For the ADIA simulations, the maximum CDNC values were reached near the model cloud base, with approximately 750, 850, and 900 cm$^{-3}$ for the 22 July, 25 July, and 1 August cases, respectively. CDNC then decreased by approximately 20–40% ~~as the parcel reached~~ across all three cases from the peak values near the model cloud base towards the cloud top, mainly due to collision–coalescence, which remained active in the ~~adiabatic~~ ADIA simulations. In contrast, for the homogeneous mixing simulations, CDNC reached a peak of approximately 650, 700, and 850 cm$^{-3}$ near the model cloud base for the three cases, respectively. At temperatures warmer than $-10$ °C, the HOM and HOM+EA simulations showed similar decreasing trends,

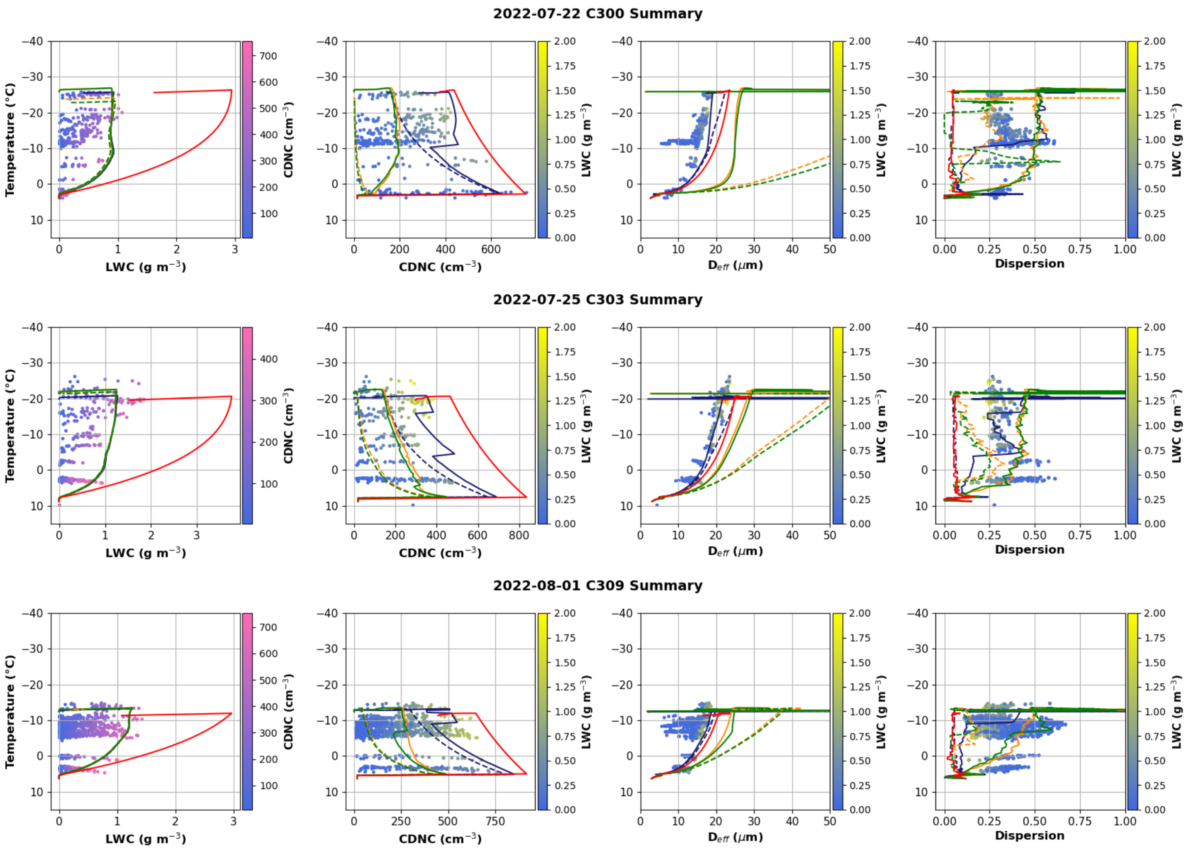

**Figure 3.** Vertical profiles of (from left to right): liquid water content (LWC), cloud droplet number concentration (CDNC), ~~liquid water content (LWC),~~ effective diameter ($D_{\rm eff}$), and dispersion for three representative cases, C300 (22 July 2022), C303 (25 July 2022), and C309 (1 August 2022). ~~Blue~~ Coloured dots indicate observations; red lines denote ADIA; solid blue lines HOM+EA; dashed blue lines HOM; solid orange lines INHOM+EA+RA; dashed orange lines INHOM+RA; solid green lines INHOM+EA; and dashed green lines INHOM.

with CDNC in HOM+EA remaining slightly higher. Around $-10$ °C, a second CDNC peak of approximately 450, 500, and 550 cm$^{-3}$ appeared in HOM+EA, likely due to secondary droplet activation triggered by entrained aerosols. Near the model cloud top, CDNC in the HOM simulations was approximately 50% lower than in the HOM+EA simulations. Overall, the homogeneous mixing simulations with external aerosol entrainment (HOM+EA) show reasonable agreement with the upper envelope ~~(yellow region)~~ of the observed CDNC.

For the inhomogeneous mixing simulations, both INHOM+EA+RA and INHOM+EA ~~reproduced the average observed CDNC reasonably well, showing similar vertical trends~~were in reasonable agreement with the observed CDNC values associated with relatively low LWC, as indicated by the blue and green dots. When the entrainment of external aerosols was disabled (i.e., with EA turned off), CDNC in the INHOM+RA and INHOM simulations decreased significantly, with only a small number of droplets remaining near the model cloud top. The effect of ~~released aerosol (RA )~~ RA on CDNC under inhomogeneous mixing conditions was found to be limited, whereas the ~~entrained aerosol (EA )~~ EA significantly enhanced CDNC. This is likely because released aerosols form in regions of evaporation, where decreasing relative humidity and strong sub-saturation prevents them from reaching the critical supersaturation required for activation. Among the inhomogeneous mixing simulations, INHOM+EA+RA showed reasonable agreement with the average observed CDNC.

~~Although the reduction in droplet number concentration under certain mixing conditions may slightly affect the efficiency of condensational growth, the overall impact on LWC remains limited. However, the ADIA simulationssignificantly overestimate LWC compared to observations, producing peak values approximately three times higher than those from simulations that include entrainment. As expected,~~ The evolution of $D_{\mathrm{eff}}$ within the parcel for the different simulations is shown in the middle-right panel of Figure 3. Across all simulations, $D_{\mathrm{eff}}$ generally increased with decreasing temperature as ~~cloud developed. The~~ the cloud developed, as a result of continued droplet growth by collision–coalescence, and reached maximum values near the cloud top. For the ADIA simulations, maximum $D_{\mathrm{eff}}$ values reached approximately 22, 29, and 23 $\mu$m for the 22 July, 25 July, and 1 August cases, respectively. In contrast, the HOM+EA simulations ~~closely followed~~ provided the best agreement with the observations, closely following the upper envelope~~of the observations. In contrast,~~, with peak $D_{\mathrm{eff}}$ values of approximately 18, 21, and 19 $\mu$m for the three cases. It is worth noting that, in the 25 July case, a pronounced increase in large droplets was observed near cloud top at temperatures of approximately $-15$ to $-20\,^{\circ}$C, and a similar feature was reproduced by the HOM+EA simulations. Overall, the inhomogeneous mixing simulations produced larger $D_{\mathrm{eff}}$ values than both the homogeneous mixing and ADIA simulations. This effect was particularly evident under inhomogeneous mixing without any entrained aerosol or aerosol recycling, where $D_{\mathrm{eff}}$ ~~reached unrealistically high values~~ became significantly larger, likely due to the ~~dominance of a small number of large droplets . In these simulations, peak $D_{\mathrm{eff}}$ values reached approximately 90, 100, and 40$\mu$m in the three cases, respectively~~removal of smaller droplets during inhomogeneous mixing, which shifted the droplet size distribution towards fewer but larger droplets.

### 4.2 Comparison of Observed and Modeled DSDs

~~The drop size distributions (DSDs) and corresponding dispersion~~ Figures S6–S8 show the observed and simulated DSDs for three representative ~~cases (~~DCMEX cases, 22 ~~-~~July, 25 ~~-~~July, and 1 ~~-August) were simulated and compared with in-situ aircraft observations. Figures S11–S13 show the vertical profiles of DSDs~~ August, at nine selected temperature levels ~~, from the~~ from cloud base to ~~the cloud top, for each case. In the 22 July case~~cloud top. In all three cases, the observed ~~$D_{\mathrm{eff}}$ increased from approximately 16 $\mu$m at –5.0 °C to 19 $\mu$m at –25.2 °C, consistent with condensational and collisional droplet growth during ascent. Meanwhile, the dispersion generally increased with height, indicating a progressive~~ DSDs showed clear broadening with height, and bimodal, or even trimodal, structures were found at some temperature levels. This broadening of the ~~droplet size distribution as the cloud developed. Similar trends were also found in the 25 July and 1 August cases.~~

~~The right panels of Figure 3 show the simulated and observed dispersions for the three cases. The dispersion is smaller within the approximate~~ DSD is also reflected in the dispersion, as shown in the right panel of Figure 3. The observed dispersion was generally smaller under higher-LWC conditions, which approximately correspond to cloud-core regions~~(yellow dots), around~~

~~0.2–0.3 near the observed cloud top, whereas larger values are found near the cloud edges (bluedots).~~ , and larger under lower-LWC conditions, shown in blue, which are more representative of cloud-edge regions.

This pattern suggests that the droplet distributions are likely broadened by entrainment, mixing, or turbulence. It should also be noted that some broadening in the observed DSDs may ~~appear more dispersed than they actually are due to instrumental effects~~ arise from measurement uncertainties, as discussed by Lance et al. (2010a). This is consistent with Faber et al. (2018), who found that the mean diameters generally agree within a few percent, whereas the median diameters are overestimated by about 5–15%, resulting in an artificial broadening and skewing of the spectra. Overall, ADIA and HOM simulations both show narrow DSDs, whereas the HOM+EA simulation reproduces key observed features of the in-situ DSDs, including a broader spectral width, the persistence of small droplets at higher altitudes, and a bimodal structure, which highlights the role of entrainment in DSD broadening, consistent with Lasher-Trapp et al. (2005) and Morrison et al. (2022a).

The results show that homogeneous mixing (HOM+EA) alone cannot explain the observed droplet dispersion, particularly ~~during the early stages of cloud development~~at the lower levels of the cloud. In contrast, inhomogeneous mixing (INHOM+EA+RA) can generate sufficiently broad droplet spectra but tends to overestimate the presence of large droplets, producing excessively wide distributions. This suggests that real cloud evolution may involve an initial inhomogeneous phase followed by more homogeneous mixing (Wu et al., 2025b). For the 22 July case, additional simulations were performed, applying INHOM+EA+RA followed by HOM+EA to examine the influence of early inhomogeneous mixing on cloud development. As shown in Fig. 4, when the inhomogeneous phase lasts less than 30 s, the simulated results approach those of fully homogeneous mixing, while durations longer than 30 s result in behaviour consistent with inhomogeneous mixing. However, a major limitation of the parcel model in this study is its simplified treatment of ascending thermal trajectories. The model assumes isolated and internally uniform parcels, whereas in real thermals, parcel trajectories evolve dynamically, with varying turbulence, humidity, and mutual entrainment between neighbouring parcels. The transition from inhomogeneous to homogeneous mixing applied here should therefore be regarded as an idealised approximation.

### 4.3 Observed and Simulated Ice-Phase Properties

~~We performed simulations for three representative casesunder three typical mixing scenarios (~~Figure 5 shows box plots of observed ice number concentration in different temperature intervals for the three selected cases, based on CPI data. Representative CPI images for each case are shown in Figs. S15–S17. To further assess and quantify the impact of SIP on ice number concentration, SIP-off and SIP-on simulations are also shown for the three model configurations, ADIA, HOM+EA, and INHOM+EA+RA, with dashed and solid lines denoting simulations without SIP, referred to here as $N_{\mathrm{INP}}$, and ~~ADIA), as shown in Figures **??**–**??**. For each scenario, the simulations including all SIPmechanisms (RS, CB, M1, and M2) were compared with the corresponding control simulations without SIP,~~ with SIP, referred to here as $N_{\mathrm{ICE}}$, respectively. We also examine the temporal evolution of ice enhancement (here defined as $N_{\mathrm{ICE}} - N_{\mathrm{INP}}$) for six entrainment simulations together with the ~~observations, to quantify~~ adiabatic reference, as shown in Fig. 6.

To assess the impact of SIP on ~~convective clouds during DCMEX~~ice number concentration, it is first necessary to establish the representation of primary ice production. In this study, ~~heterogeneous freezing~~ primary ice production was parame-

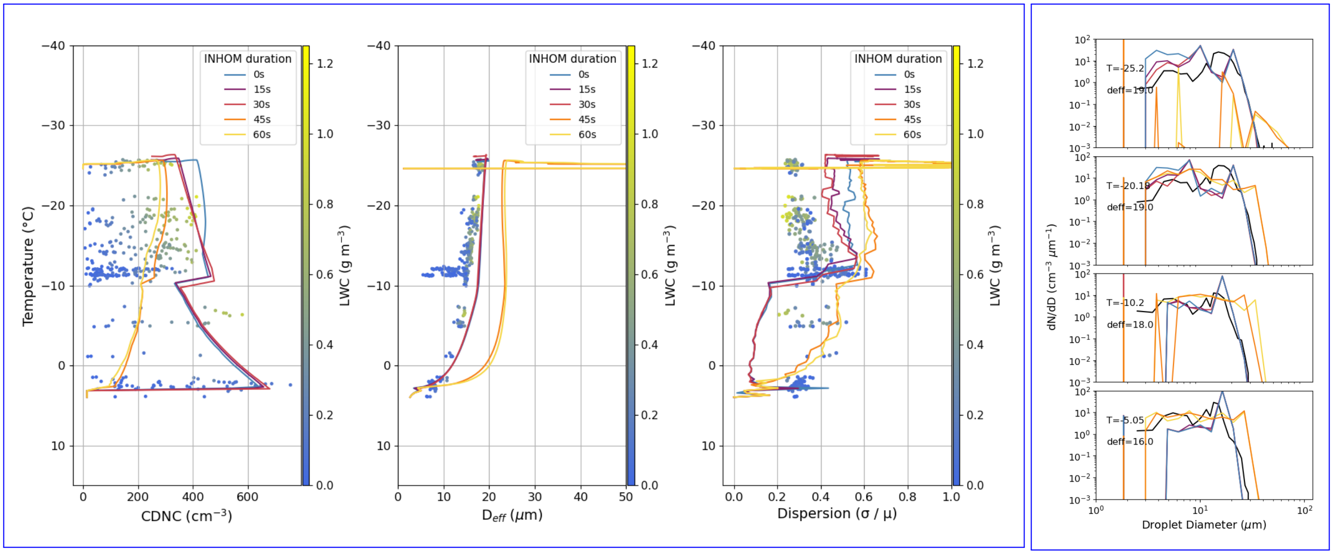

**Figure 4.** Vertical profiles of observed and simulated CDNC (left), $D_{\mathrm{eff}}$ (centre-left), and dispersion (centre-right), together with droplet size distributions (right) at four selected temperatures for the 22 July 2022 case. *INHOM duration* indicates the period of the INHOM+EA+RA phase in the combined INHOM+EA+RA–HOM+EA simulation.

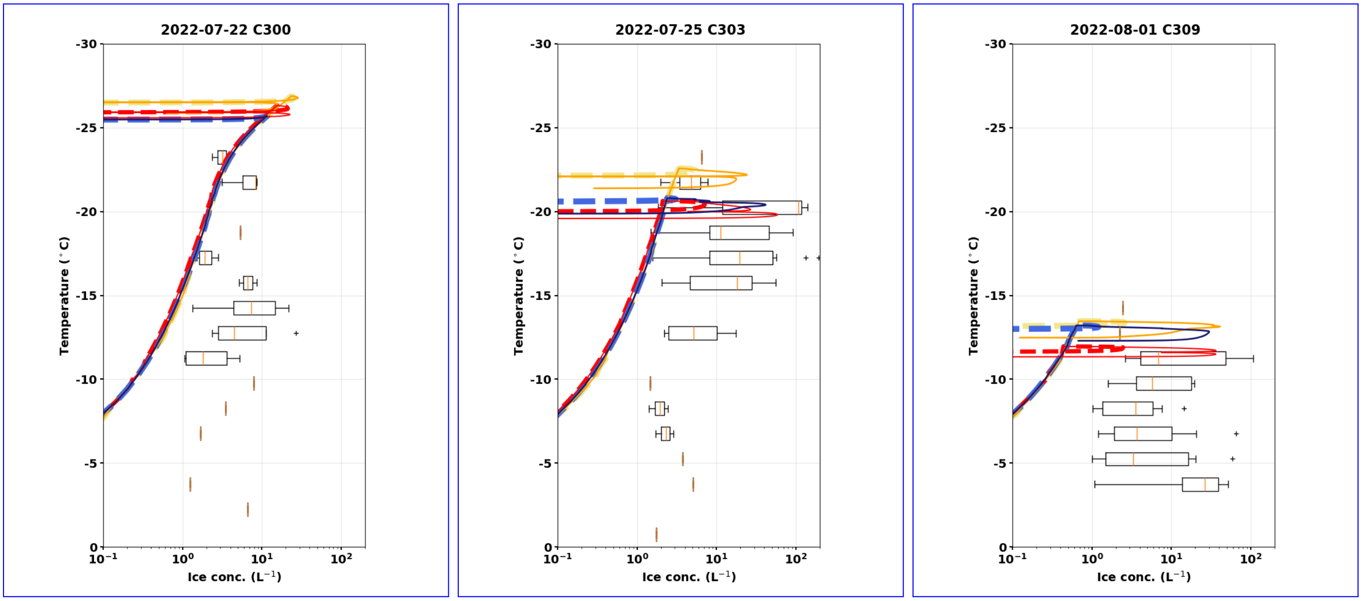

**Figure 5.** Observed and simulated ice particle concentrations as a function of temperature for the three selected cases. In each panel, the boxplots show the observed ice concentrations based primarily on CPI data, and the coloured lines show the parcel model simulations under different entrainment scenarios. Blue, orange, and red lines represent the HOM+EA, INHOM+EA+RA, and ADIA simulations, respectively. Solid lines represent simulations with all SIP mechanisms activated, while dashed lines indicate simulations with SIP processes disabled.

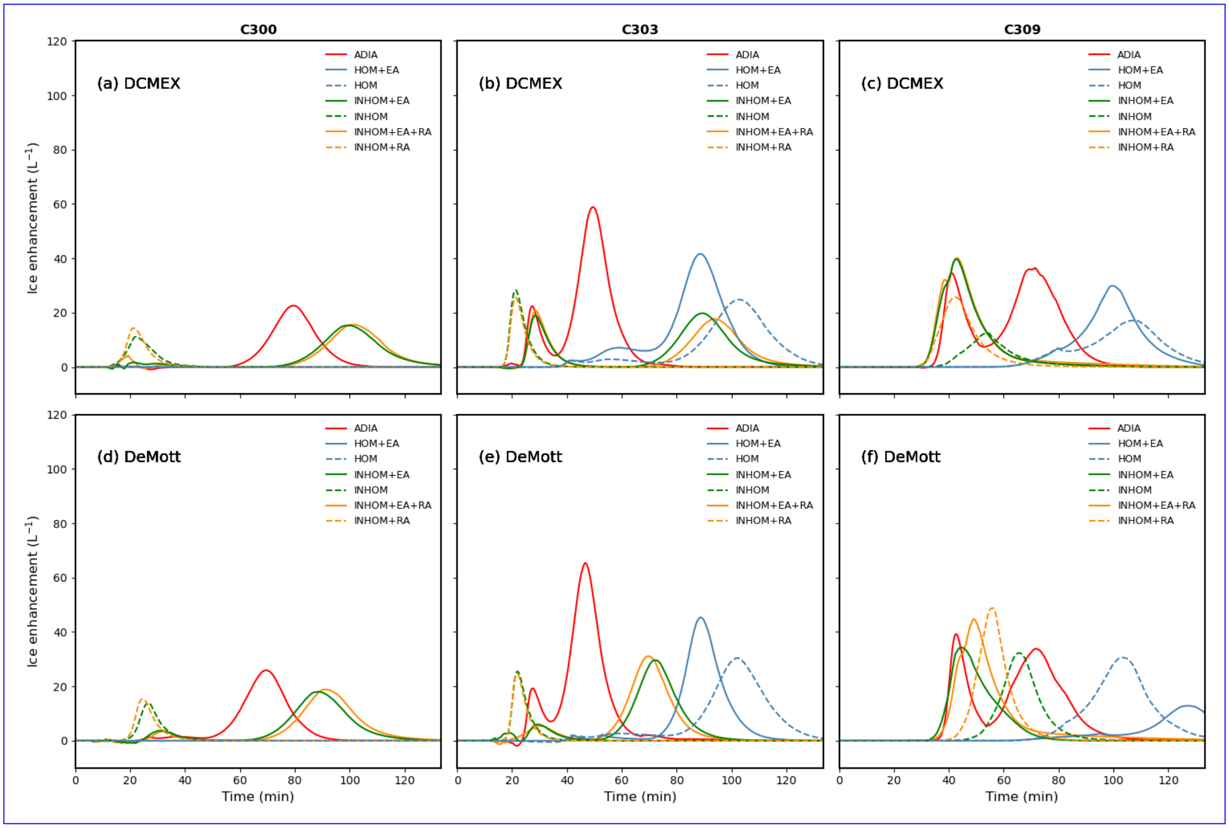

**Figure 6.** Time series of ice enhancement for three representative cases: C300 (left), C303 (middle), and C309 (right). The top row (a–c) shows simulations using the heterogeneous freezing parameterisation of Daily et al. (2025), while the bottom row (d–f) shows results using the parameterisation of DeMott et al. (2010). Colour coding follows Fig. 3.

terised following ~~?, and the simulated ICNC values were overall~~ Daily et al. (2025). The resulting $N_{\mathrm{INP}}$ profiles from the different model configurations, plotted as dashed lines in Fig. 5, were broadly consistent with the INP curve ~~reported by ?. The parameterisation of DeMott et al. (2010) was also tested for comparison, and the results showed only minor differences~~ shown in the right panel of Fig. S2. For comparison, we also tested the parameterisation of DeMott et al. (2010). Only minor differences in ice enhancement were found between the two ~~schemes.~~parameterisations, as shown in the upper and lower panels of Fig. 6.

~~Vertical profiles of ice particle concentration and corresponding CPI imagery for the 22 July 2022 (C300) case. The left panel shows the observed (boxplots) and simulated ice concentrations from the parcel model under different entrainment scenarios, shown as a function of temperature. Blue, orange, and red lines represent the HOM+EA, INHOM+EA+RA, and ADIA simulations, respectively. Solid lines represent simulations with all SIP mechanisms activated, while dashed lines indicate simulations with SIP processes disabled. The right panel presents representative CPI images of ice particles sampled at approximately −8 °C, −12 °C, and −23 °C.~~

For the 22 July case, ~~the control ICNC~~ as shown in the left panel of Fig. 5, $N_{\mathrm{INP}}$ peaked at approximately 20 ~~$\mathrm{L}^{-1}$~~, 10 ~~$\mathrm{L}^{-1}$~~, and 25 $\mathrm{L}^{-1}$ ~~around 20 min~~ near $-26\,^{\circ}\mathrm{C}$ in the ADIA, HOM+EA, and INHOM+EA+RA simulations, respectively. ~~As shown in Fig. ??,~~ HOM+EA produced almost no ice enhancement, whereas both ADIA and INHOM+EA+RA showed increases of about 20 $\mathrm{L}^{-1}$~~(see the left panel of Fig. 7), with SIP in INHOM+EA+RA occurring roughly 20 minlater than in ADIA. The simulated profiles need to be shifted downward to match the observations, likely because all particles remain within a single parcel without downdrafts or multiple thermals. In reality, ice particles are vertically transported, representing another limitation of the BMM framework.Similarly, for the 25 July~~ , occurring at around 80 and ~~1 August cases, the model underestimated ice concentrations below $-20\,^{\circ}\mathrm{C}$, mainly because the simplified parcel representation cannot capture the ongoing vertical transport of ice particlesin real clouds.~~

~~For the south-easterly flow cases (25 July and 1 August), the control ICNCs were low, about 6 and 2 $\mathrm{L}^{-1}$, respectively, and could not explain the observed ice concentrations. Only when SIP mechanisms were activated did the simulations reproduce the observed magnitudes, showing reasonable agreement with the measurements~~100 min, respectively, as shown in panel a of Fig. 6. Figure S15 shows representative CPI images for the 22 July case. Near $-8\,^{\circ}\mathrm{C}$, the images were dominated by small, rounded particles, which are likely to be droplets. No obvious large droplets or well-developed ice crystals were observed at this temperature. At colder levels, some larger and more irregular ice particles were present. However, these were relatively few, and the particle population remained dominated overall by small, rounded particles.

For the 25 July case, panel (b) of Fig. 6 shows that ADIA, HOM+EA, and INHOM+EA+RA produced ice enhancement at around 50, 90, and 95 min, reaching approximately 60, 40, and 20 $\mathrm{L}^{-1}$, respectively. ~~In the adiabatic simulation (ADIA ), two peaks occurred~~ ADIA showed two peaks at about 25 and 50 min, with maxima of roughly 20 and 60 $\mathrm{L}^{-1}$. ~~The homogeneous mixing simulation (HOM ) produced~~ HOM showed a single peak of about 35 $\mathrm{L}^{-1}$ near 105 min, whereas HOM+EA peaked earlier~~(~~, at around 90 min~~) at~~ , with a maximum of about 45 $\mathrm{L}^{-1}$. In contrast, ~~both~~ INHOM+RA and INHOM+EA+RA ~~showed~~ both exhibited two peaks, at approximately 25 and 90 min, each reaching about 20 $\mathrm{L}^{-1}$. Figure S16 shows representative CPI images for the 25 July case. At approximately $-8\,^{\circ}\mathrm{C}$, the available CPI images were consistently dominated by rounded particles, with diameters mainly between 35 and 45 $\mu$m. No obvious faceted ice crystals were observed. At $-16,^{\circ}\mathrm{C}$, larger rounded particles became clearly visible, with diameters generally exceeding 100 $\mu$m, and are inferred to represent large droplets. This may reflect the relatively warm cloud base in the 25 July case, which would provide sufficient liquid water for the droplets to grow to larger sizes before reaching colder levels. Potential inhomogeneous mixing may also have promoted a broader droplet size distribution, favouring the formation of larger droplets. In the representative CPI images shown for this temperature, irregular particles and some larger ice crystals were also visible, including hexagonal crystals, columnar crystals, and their aggregates. The red-boxed region may indicate a possible droplet–ice collision event, together with the presence of several small ice crystals and small supercooled raindrops in the surrounding area over a short period. At $-22\,^{\circ}\mathrm{C}$, larger droplets and irregular ice crystals were still observed, and partially developed hexagonal ice crystals were also present.

For the 1 August case, panel (c) of Fig. 6 shows that ADIA produced two peaks at around 40 and 70 min, both ~~near~~ reaching approximately 40 $\mathrm{L}^{-1}$. INHOM+RA and INHOM+EA+RA also exhibited early ~~enhancement at~~ ice enhancement at around 40 min, ~~reaching similar magnitudes. The homogeneous simulations showed later peaks, with HOM reaching about 20~~with their peak timing close to that of the first ADIA peak. HOM+EA reached a peak of about 40 L$^{-1}$ at ~~110~~approximately 100 min, ~~and HOM~~whereas the HOM peak occurred about 10 min later and reached only around 20 L$^{-1}$. Notably, the result for HOM and HOM+EA ~~slightly earlier at 100 min with a maximum of 38 L$^{-1}$.~~ was reversed in panel (f), where HOM showed greater ice enhancement and reached its peak earlier than HOM+EA. Figure S17 shows representative CPI images for the 1 August case. At approximately $-5\,^{\circ}$C, relatively large particles were observed, with sizes reaching 300 to 400 $\mu$m. Columnar ice crystals and some small irregular ice particles were also present. At approximately $-8\,^{\circ}$C, small supercooled raindrops were observed, while the images were dominated by aggregated ice particles, with the largest particle exceeding 500 $\mu$m in diameter. At the colder sampled level, at about $-11\,^{\circ}$C, few obvious ice crystals were observed, and the images were dominated mainly by smaller supercooled raindrops.

~~Vertical profiles of ice particle concentration and corresponding CPI imagery for the 25 July 2022 (C303) case. The left panel shows the observed (boxplots) and simulated ice concentrations from the parcel model under different entrainment scenarios, shown as a function of temperature. Coloured lines are as defined in Figure **??**. The right panel presents representative CPI images of ice particles sampled at approximately $-8\,^{\circ}$C, $-16\,^{\circ}$C, and $-22\,^{\circ}$C.~~ It is worth noting that, for the three selected cases, the ice number concentrations simulated near the modelled cloud top when SIP was included were generally consistent with the observed ice number concentrations near the highest aircraft passes. However, at warmer levels during parcel development, the simulated ice concentrations were less consistent with the observations (Fig. 5). This likely reflects limitations of the BMM as a one-dimensional model, which will be discussed in more detail in the Discussion section.

~~Vertical profiles of ice particle concentration and corresponding CPI imagery for the 1 August 2022 (C309) case. The left panel shows the observed (boxplots) and simulated ice concentrations from the parcel model under different entrainment scenarios, shown as a function of temperature. Coloured lines are as defined in Figure **??**. The right panel presents representative CPI images of ice particles sampled at approximately $-5\,^{\circ}$C, $-8\,^{\circ}$C, and $-11\,^{\circ}$C.~~

~~Time series of ice enhancement for three representative cases: C300 (left), C303 (middle), and C309 (right). The top row (a–c) shows simulations using the heterogeneous freezing parameterisation of **?**, while the bottom row (d–f) shows results using the parameterisation of DeMott et al. (2010). Colour coding follows Fig. 3.~~

### 4.4 Analysis of Individual SIP Mechanisms

~~Sensitivity tests were conducted~~ Figure 7 presents sensitivity tests for all three cases~~to assess~~, designed to isolate the individual contribution of the four SIP mechanisms~~(~~, RS, CB, M1, and M2~~).~~. Primary ice formation was parameterised using Daily et al. (2025) in all simulations. In each test, only one SIP mechanism was activated, while the other three were switched off. Overall, RS and M1 were largely inactive and produced little ice enhancement in all three cases. By contrast, M2 was active in all cases, whereas CB was only active and produced ice enhancement in the 1 August case.

For the 22 July case, ~~RS~~ when RS was activated, only INHOM+EA+RA produced a small ice enhancement of about 5 L$^{-1}$ ~~only in the INHOM+EA+RA simulation, occurring~~ at around 20 min. ~~Most SIP activity appeared in the later stage of cloud development, when the parcel top temperature dropped below $-25^{\circ}$C. RS conditions were not met when~~ The available CPI images within the temperature range favourable for RS also show no clear large rimed particles (Fig. S15).

When M1 was activated, only the inhomogeneous mixing simulations showed a very small ice enhancement during the first 20 min of the simulation, reaching about 7 $\mathrm{L}^{-1}$. When M2 ~~conditions were active, and only M2 produced a noticeable ice increase~~was activated, no ice enhancement was observed in the homogeneous simulations. In contrast, ADIA produced a peak ice enhancement of about 20 $\mathrm{L}^{-1}$ at around 80 min, while INHOM+EA and INHOM+EA+RA produced ice enhancements of about 18 $\mathrm{L}^{-1}$ at around 100 min.

For the 25 July case, ~~ice enhancement is likewise only observed when~~ no clear ice enhancement was produced when RS, CB, or M1 was activated individually. When M2 ~~is activated. In the inhomogeneous simulations without aerosol release (~~was activated, ADIA showed a double peak, reaching about 20 and 40 $\mathrm{L}^{-1}$ at around 30 and 50 min, respectively. The ice enhancements in INHOM and INHOM+~~EA), large droplets appear early in the simulation, leading to ice enhancement around 20 min with peak values of approximately 20 $\mathrm{L}^{-1}$~~RA occurred at times similar to the first peak in ADIA. By contrast, ~~the~~ HOM+EA~~and the inhomogeneous simulations with aerosol release (~~, INHOM+EA~~+RA~~ , and INHOM+~~RA) exhibit delayed ice enhancement, occurring at around 95 min with peak values~~ EA+RA reached peak ice enhancements of about 40 ~~$\mathrm{L}^{-1}$~~, 20, and 20 ~~$\mathrm{L}^{-1}$, respectively. When entrainment of aerosols is not considered (HOM ), the onset of ice enhancement is further delayed, appearing roughly 20~~$\mathrm{L}^{-1}$, respectively, at around 85 min. HOM peaked about 10 min later ~~and reaching peak values of around 30 $\mathrm{L}^{-1}$. As shown in the right panel of~~ than HOM+EA, and its peak ice enhancement was only about 25 $\mathrm{L}^{-1}$. In the CPI images for the 25 July case shown in Fig. ~~??, the CPI image displays a typical hexagonal crystal in the upper-right corner, likely formed after an ice –ice collision . The red box highlights features~~ S16, both large droplets and large ice particles were frequently observed, providing favourable conditions for M2. Within the red boxed region, a possible droplet–ice collision is visible, with numerous small ice crystals observed close to the possible collision feature. This feature is consistent with fragmentation ~~between supercooled droplets and~~ during the freezing of supercooled droplets upon collision with a more massive ice ~~particles (Mode 2).~~ particle, and this provides observational evidence that M2 may have occurred in this case. In addition, at around $-22,^{\circ}$ C, partially broken ice crystals with an incomplete hexagonal shape were observed. These features may reflect mechanical damage associated with ice–ice collisions, and could suggest a minor contribution from CB.

For the 1 August case, ~~RS produced no noticeable~~ no ice enhancement was observed when RS or M1 was activated individually. When CB was activated, ADIA showed no ice enhancement, ~~as expected. In the~~ whereas INHOM+EA and INHOM+~~RA, ADIA, and HOM+~~EA~~simulations, M2 generated~~ +RA produced ice enhancements of ~~approximately 25, 40, and~~ about 15 $\mathrm{L}^{-1}$ at around 65 min. HOM+EA and HOM reached about 30 and 15 $\mathrm{L}^{-1}$ at around ~~40, 80,~~ 100 and 110 min, respectively. When ~~only the CB mechanism~~ M2 was activated, ADIA showed a double peak, with ice enhancement occurring at around 40 and 75 min. The inhomogeneous mixing simulations produced ice enhancement at times similar to the first ADIA peak, while HOM+EA and ~~INHOM+EA+RA showed additional ice enhancement of~~ HOM reached about 30 and ~~20~~25 $\mathrm{L}^{-1}$ at around ~~100 and 70~~110 and 115 min, respectively. This is consistent with the CPI images shown in Fig. S17, in which large ice particles and relatively large droplets were frequently observed, providing favourable conditions for both M2 and CB.

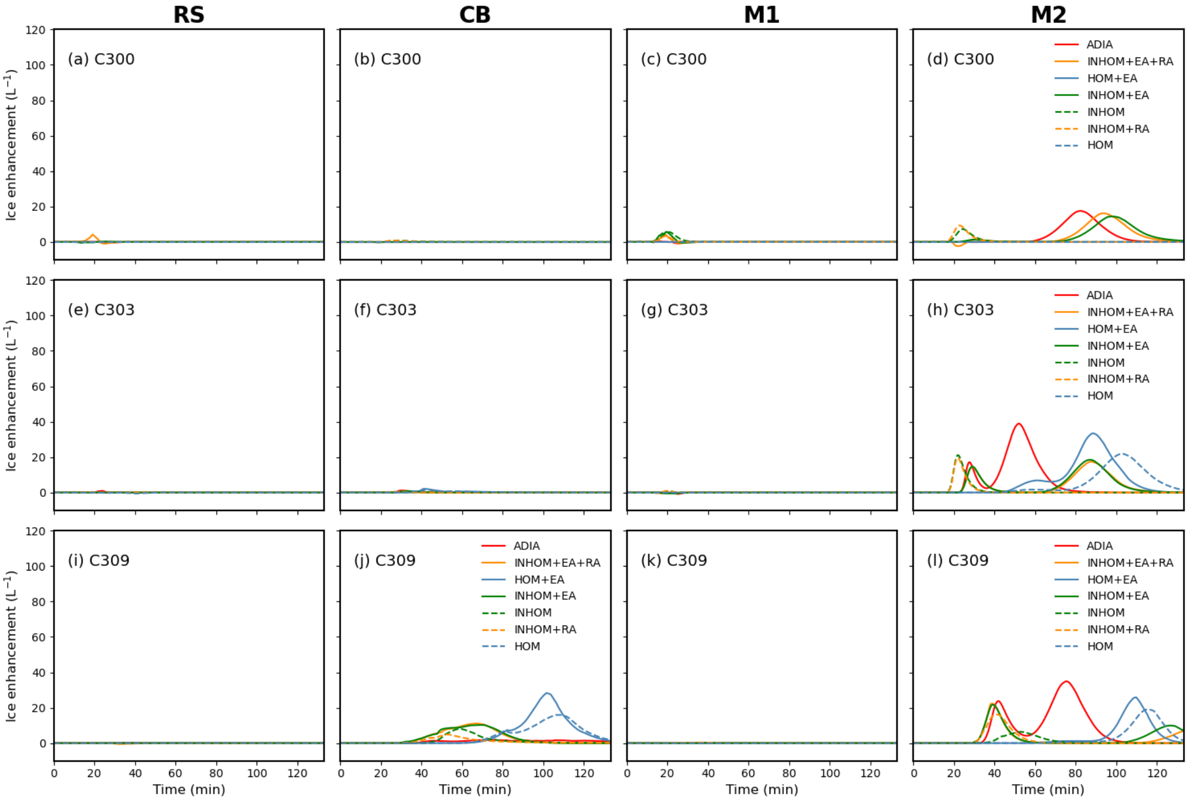

**Figure 7.** Time series of ice enhancement from individual SIP mechanisms for three representative cases: ~~C300~~ 22 July (C300, top row), ~~C303~~ 25 July (C303, middle row), and ~~C309~~ 1 August (C309, bottom row). Panels show the results for RS (a, e, i)~~rime splintering (RS)~~, CB (b, f, j)~~collisional breakup (BR)~~, M1 (c, g, k)~~mode 1 freezing fragmentation (M1)~~, and M2 (d, h, l)~~mode 2 droplet–ice fragmentation (M2)~~. Colour coding follows Fig. 3.

## 5 Discussion

In our study, we investigated four SIP mechanisms (RS, CB, M1, and M2) in 15 deep convective cloud cases observed during the DCMEX campaign from 22 July to 7 August 2022 using a parcel model. Two entrainment representations (homogeneous and inhomogeneous mixing) were incorporated into the model, extending the adiabatic framework of James et al. (2023) to better represent dilution effects on cloud microphysics. Our results suggest that M2 is likely a key mechanism for explaining the high ice particle concentrations observed in deep convective clouds during the DCMEX campaign (see Figs. S6–S10). As for the other mechanisms, RS and M1 remained largely inactive across all 15 cases, ~~while~~ whereas CB contributed to ice enhancement in ~~some shallower cloud cases . M1 was likely not effective because collisions between large supercooled droplets and small ice crystals were rare, as shown by the CPI observations (Figs. 5–7).~~ cases with warm cloud-top temperatures, as illustrated by the 1 August case (C309; Fig. S8). It should be noted that RS may be underestimated in ~~a~~ our parcel model (see discussion later). However, observations during DCMEX indicate that RS contributed little to SIP in these clouds. This may partly result from the flight pattern adopted during the campaign, which could have limited sampling of regions where RS was active (P. J. Connolly, personal communication). The entrainment of aerosol was also found to accelerate the collision–coalescence process under homogeneous mixing conditions, leading to earlier ice enhancement, consistent with the hypothesis proposed by James et al. (2023).

To investigate the role of each SIP mechanism, it is first necessary to examine the development of the liquid phase during the early stages of cloud evolution. In our simulations, large droplets with diameters greater than 150 $\mu$m are critical for initiating M2, since droplets of this size with higher relative velocities are more likely to produce splashing during collisions. M2 becomes more active as the ratio of collision kinetic energy to surface energy increases in our BMM (Phillips et al., 2018a; James et al., 2023). Previous studies have also shown that different representations of liquid-phase microphysics, especially the contrast between bulk and bin schemes (Lee and Baik, 2018; Johnson et al., 2024), can substantially affect the simulated efficiency of SIP. Grzegorczyk et al. (2025) and Qu et al. (2022) both analysed the same observational case of tropical deep convective clouds from the HAIC/HIWC campaign but reached contrasting conclusions regarding the contribution of ~~droplet shattering~~ DS (corresponding to our M1+M2) to ice enhancement, which they indicate differences in the availability of large droplets.

We found that representing aerosol entrainment was essential for simulating the observed breadth of the droplet size distribution during the DCMEX campaign. The observations revealed a bimodal spectrum with a distinct minimum near 10$\mu$m, suggesting the presence of a secondary activation mechanism. This type of distribution has also been reported in previous studies (Morrison et al., 2022a; Chandrakar et al., 2021a; Cooper et al., 2013). James et al. (2023) also employed a parcel model to investigate the role of M2 in idealised shallow convective clouds. Their modelling setup is similar to our adiabatic configuration. Although adiabatic assumption can sometimes provide a reasonable approximation, observational and ~~LES~~ large-eddy simulation (LES) studies have shown that entrainment can begin almost immediately after cloud formation, with turbulent mixing potentially diluting the parcel even within a few hundred metres above cloud base (Grabowski and Wang, 2013). We found that the adiabatic simulations produced narrower droplet size distributions and tended to substantially overestimate CDNC, as well as LWC by up to approximately 300 %. As a result, the efficiency of ~~secondary ice production~~ SIP was also overestimated, in some cases with relatively warm cloud-base temperatures and deeper cloud layers, such as C306 and C312 (see Fig. S14), the enhancement of ice production was even two to three times greater than in the simulations that included entrainment. Simulations with inhomogeneous mixing tend to lead to an underestimation of CDNC and an overestimation of $D_{\mathrm{eff}}$, as shown in Fig. 3. Although many previous studies suggest that inhomogeneous mixing tends to become more prevalent during later stages of the cloud life cycle, this is likely due to increased entrainment and evaporation near the cloud edges as the updraft weakens (e.g. Lehmann et al., 2009; Lim and Hoffmann, 2024; Xu et al., 2022). We did not find evidence supporting its dominance in our cases. This may be due to the aircraft tracking the developing clouds, thereby sampling them during the early stages of their lifecycle.

Despite the potential importance of entrainment for SIP, they have rarely been systematically evaluated in existing studies. Georgakaki et al. (2022) used the mesoscale model WRF with the Morrison double-moment microphysics scheme to investigate three SIP mechanisms, RS, CB and ~~droplet shattering~~ DS (corresponding to our M1 and M2) in two alpine clouds. They found CB to be the dominant contributor to SIP, while DS was inactive, likely due to the lack of large droplets. However, the Morrison double-moment scheme in WRF is closer to the homogeneous mixing limit in its evaporation–dilution representation. In our colder cloud-base case (C300), homogeneous mixing likewise produced no active SIP, whereas M2 became active under inhomogeneous mixing due to the production of large droplets. This suggests that the efficiency of DS in Georgakaki et al. (2022) may have been underestimated. A broad droplet size distribution can accelerate warm-rain formation through collision and coalescence, which can therefore affect SIP. Our results show that, across all SIP-active cases, HOM+EA leads to secondary ice enhancement occurring 15–20 minutes earlier and increasing in magnitude by approximately 30–40% compared with HOM. Sotiropoulou et al. (2020) used a high-resolution LES with double-moment bulk microphysics and explicitly resolved turbulent entrainment to investigate the effects of ~~HM, BR~~ RS, CB and droplet fragmentation on summer Arctic stratocumulus. However, even at such high resolutions, the grid-scale microphysics in these models typically assumes instantaneous homogeneous mixing (e.g., Morrison and Grabowski, 2008). They found DS to be ineffective, yet this assumption cannot resolve the detailed evolution of the droplet size distribution under local dilution and may underestimate spectral broadening caused by size-dependent evaporation, potentially leading to an underestimation of DS.

In ~~an~~ this study, ice particle observations were primarily based on the processed CPI ice concentration variable, together with CPI imagery. The CPI imagery remains valuable for identifying larger particles and particle habits, and therefore for supporting the interpretation of SIP, as discussed in Sect. 4.4. For the three cases analysed in this study, the CPI images suggest that the coexistence of large droplets with small ice crystals was relatively uncommon, whereas coexistence with larger ice particles was observed more frequently, indirectly suggesting from an observational perspective that M1 may have been relatively inactive in these clouds, while M2 may have played a more important role. However, it should be acknowledged that the relatively limited sample volume of the CPI means that the inferred number concentrations are more strongly influenced by sampling noise, particularly when particle concentrations are low or spatial variability is pronounced (Baumgardner et al., 2017; McFarquhar et al., 2017). Further study including a more complete intercomparison across multiple probes would be useful to better constrain the observational uncertainty.

In an earlier study of summertime cumuli over the same region in New Mexico, Blyth and Latham (1993) observed high ice crystal concentrations. They concluded that this enhancement could be explained by the Hallett–Mossop (HM) process, based on the observed coexistence of ~~supercooled drizzle drops with radii greater~~ graupel and supercooled drops larger than 24 $\mu$m ~~and graupel~~ in diameter near the RS temperature range. However, ~~this is not supported by~~ we did not find this in our results (see Fig. ~~S11~~S10), as RS remains inactive throughout all 15 simulated cases. The clouds investigated in their study are similar to those observed during the DCMEX project in 2022. It also should be noted that the ice crystal concentrations reported by Blyth and Latham (1993) were likely significantly overestimated due to probe-induced shattering (Korolev et al., 2013; Jackson et al., 2014). In our simulations, the model results indicate that RS is not the dominant SIP mechanism in the early stage of cloud development~~(see Fig. S6).~~. We also acknowledge that the parcel model, due to its simplified structure, may underestimate the contribution of the RS mechanism. During the Ice in Clouds Experiment-Tropical (ICE-T) field campaign, Lasher-Trapp et al. (2016) reported cases in tropical maritime cumuli where graupel ascended near cloud tops and was later observed falling back into the rime-splintering zone, suggesting that RS could have been enhanced. Observations and simulations of tropical convective clouds during the Ice in Clouds Experiment-Dust (ICE-D) campaign by Cui et al. (2022) showed that ~~the HM process~~ RS was more active under multi-thermal conditions.

It should also be noted that the simplified framework of the parcel model introduces several limitations in the representation of cloud microphysical processes. The aerosol hygroscopicity parameter, $\kappa$, used in this study was calculated following the Zdanovskii–Stokes–Robinson mixing rule described by Wu et al. (2025a). The resulting bulk $\kappa$, which represents a volume-fraction-weighted average of the hygroscopicities of the individual aerosol components, was applied uniformly to all aerosol size bins. However, aerosol particles of different sizes may differ in chemical composition in the real atmosphere, and their $\kappa$ values are therefore not necessarily identical (Petters and Kreidenweis, 2007; Xu et al., 2021). Because it was derived using volume weighting, this bulk $\kappa$ value may be more reflective of the hygroscopicity of particles in the larger size bins than a number-weighted mean would be. However, applying a single $\kappa$ value to all aerosol size bins neglects size-dependent aerosol hygroscopicity, introducing uncertainty into the simulated M2 activity, which is sensitive to the formation of larger cloud droplets.

Our 1D parcel model is also more representative of the evolution of a single local ascending trajectory than of the full cloud system, in which multiple air parcels interact continuously. In the observations (e.g. Figs. S15–S17), ice crystals observed in the lower part of the cloud may not arise solely from in situ formation within a single local ascending parcel, but may also reflect contributions from ice transported from other cloud regions through vertical or lateral exchange, together with redistribution associated with turbulent entrainment and mixing. In addition, as large ice particles formed in the model cannot leave the parcel through sedimentation, the local $N_{\mathrm{ice}}$ in the upper part of the cloud may be overestimated. These results are therefore more suitable for interpreting local processes and the relative contributions of individual mechanisms than for being regarded as a complete representation of the three-dimensional ice-phase structure of the whole deep convective cloud.

To assess the impact of primary ice nucleation on SIP, we tested two INP parameterizations, ~~Daily (2025)~~ Daily et al. (2025) and DeMott et al. (2010). The former is more appropriate for this study, as it was developed from measurements in the inflow clear air below cloud bases and in the environment around clouds during the DCMEX project, whereas the latter is a more general parameterization. However, our simulations showed negligible differences in SIP efficiency between the two, suggesting that once secondary ice multiplication is triggered, the choice of INP parameterization has limited influence on the final ice particle concentrations under these convective conditions.

## 6 Conclusions

In this study, we implemented entrainment parameterisations in the bin microphysics parcel model, including two different mixing representations (homogeneous and inhomogeneous) and external aerosol entrainment. These schemes were applied to simulations of summer continental deep convective clouds over New Mexico to assess the impacts of dry air and aerosol entrainment on cloud microphysical properties and secondary ice production. The representation of entrainment leads to systematic differences in secondary ice production by modifying liquid-phase microphysical properties (e.g. cloud droplet number concentration, liquid water content, and droplet size distribution), thereby affecting both the efficiency and onset of ice enhancement.

Our results show that the observed broad and bimodal droplet size distribution can only be reproduced when entrainment is included, particularly aerosol entrainment, within the parcel model framework for individual air trajectories. This is consistent with previous studies on the effects of dilution on the warm phase of clouds. In our adiabatic parcel simulations, cloud droplet number concentration and liquid water content are much higher than in simulations that include entrainment, with liquid water content exceeding entrainment cases by up to ∼300%. As a result, ice enhancement is up to 2–3 times larger in some cases. Under homogeneous mixing, aerosol entrainment tends to result in a broader droplet size distribution, with the SIP peak occurring 15–20 min earlier and reaching a higher peak value (by about 25%) than in simulations without aerosol entrainment. For shallow cloud cases, aerosol entrainment has little impact on SIP under inhomogeneous mixing. In deep cloud cases, inhomogeneous mixing results in an early SIP maximum (within ∼20 min) associated with an excess of large droplets; however, aerosol entrainment shifts the SIP peak to a timing comparable to that under homogeneous mixing. In our simulations of the DCMEX cases over New Mexico, most cases are best represented by homogeneous mixing combined with aerosol entrainment. We also find no evidence that inhomogeneous mixing dominates in the simulated clouds, which may be due to the aircraft primarily sampling clouds during their early stages of development.

When the four SIP mechanisms (RS, CB, M1 ~~,~~ and M2) are examined separately, our results suggest that M2~~is the dominant~~ , as currently understood and represented in the model, is the most important contributor to ice enhancement in the DCMEX deep convective cloud cases. M1 remains largely inactive, likely due to limitations of the parcel model in which the absence of sedimentation leads to an accumulation of ice crystals and a progressive reduction in supercooled liquid water, thereby suppressing collisions between large droplets and small ice crystals required for efficient M1. CB contributes to ice enhancement in some shallower cloud cases but produces little ice enhancement in the deeper cloud cases. Our results suggest that RS alone cannot account for the high ice crystal concentrations observed during DCMEX. This contrasts with earlier interpretations for summertime cumuli over the same region, which attributed ice enhancement mainly to the Hallett–Mossop process (Blyth and Latham, 1993). In our simulations, RS is inefficient during the early stages of cloud development because the temperature range favourable for rime splintering does not coincide with the presence of sufficiently large droplets and ice particles. The contribution of RS may be underestimated in the parcel model framework, as multi-thermal circulations and interactions between different air parcels are not represented. Future extensions of the model that include sedimentation and interactions between different air parcels will therefore be required to better assess the potential role of RS in deep convective clouds.

Further progress in understanding M2 will require improved laboratory constraints on freezing-drop fragmentation and continued development of idealised parcel modelling frameworks that include sedimentation and interactions between different air parcels. Incorporating the effects of entrainment on secondary ice production will also be critical for achieving an accurate representation of ice-phase processes in numerical weather prediction and other large-scale models.

*Code and data availability.* The University of Manchester bin microphysics parcel model is available upon request. The model output data generated in this study will be deposited in Figshare, a FAIR-aligned (findable, accessible, interoperable and re-usable) data repository, and made publicly available upon acceptance of the manuscript.

*Author contributions.* BZP and PJC conceived the original study. PJC developed the model code. BZP performed the simulations, analysed the data, and wrote the manuscript. HW provided key observational data. PJC, AMB and RLJ contributed to scientific discussions and provided comments on the manuscript.

*Competing interests.* The authors declare that they have no conflict of interest.

*Acknowledgements.* Airborne data were obtained using the FAAM Airborne Laboratory BAe-146 Atmospheric Research Aircraft, operated by Airtask Ltd, managed by the National Centre for Atmospheric Science, leased through the University of Leeds, and owned by UK Research and Innovation and the Natural Environment Research Council.

This project (author PJC) has received funding from the Horizon Europe programme under Grant Agreement No. 101137680.

The author used ChatGPT to assist with language editing and improving the clarity of the manuscript. All scientific analysis, interpretations, and conclusions were performed by the authors.

# References

Abel, S. J., Cotton, R. J., Barrett, P. A., and Vance, A. K.: A comparison of ice water content measurement techniques on the FAAM BAe-146 aircraft, Atmospheric Measurement Techniques, 7, 3007–3022, https://doi.org/10.5194/amt-7-3007-2014, 2014.

Adams, D. K. and Comrie, A. C.: The north American monsoon, Bulletin of the American Meteorological Society, 78, 2197–2214, 1997.

Adams, D. K. and Souza, E. P.: CAPE and convective events in the Southwest during the North American monsoon, Monthly Weather Review, 137, 83–98, 2009.

Baker, M. B., Corbin, R. G., and Latham, J.: The influence of entrainment on the evolution of cloud droplet spectra: I. A model of inhomogeneous mixing, Q. J. R. Meteorol. Soc., 106, 581–598, https://doi.org/https://doi.org/10.1002/qj.49710644914, 1980.

Baumgardner, D., Abel, S., Axisa, D., Cotton, R., Crosier, J., Field, P., Gurganus, C., Heymsfield, A., Korolev, A., Kraemer, M., et al.: Cloud ice properties: In situ measurement challenges, Meteorological monographs, 58, 9–1, 2017.

Billault-Roux, A.-C., Georgakaki, P., Gehring, J., Jaffeux, L., Schwarzenboeck, A., Coutris, P., Nenes, A., and Berne, A.: Distinct secondary ice production processes observed in radar Doppler spectra: insights from a case study, Atmospheric Chemistry and Physics, 23, 10 207–10 234, https://doi.org/10.5194/acp-23-10207-2023, 2023.

Blyth, A. M. and Latham, J.: Development of ice and precipitation in New Mexican summertime cumulus clouds, Quarterly Journal of the Royal Meteorological Society, 119, 91–120, https://doi.org/https://doi.org/10.1002/qj.49711950905, 1993.

Bott, A.: A flux method for the numerical solution of the stochastic collection equation, J. Atmos. Sci., 55, 2284–2293, 1998.

Brown, P. N., Byrne, G. D., and Hindmarsh, A. C.: VODE: A variable-coefficient ODE solver, SIAM journal on scientific and statistical computing, 10, 1038–1051, 1989.

Chandrakar, K. K., Grabowski, W. W., Morrison, H., and Bryan, G. H.: Impact of Entrainment Mixing and Turbulent Fluctuations on Droplet Size Distributions in a Cumulus Cloud: An Investigation Using Lagrangian Microphysics with a Subgrid-Scale Model, Journal of the Atmospheric Sciences, 78, 2983 – 3005, https://doi.org/10.1175/JAS-D-20-0281.1, 2021a.

Chandrakar, K. K., Grabowski, W. W., Morrison, H., and Bryan, G. H.: Impact of entrainment mixing and turbulent fluctuations on droplet size distributions in a cumulus cloud: An investigation using Lagrangian microphysics with a subgrid-scale model, Journal of the Atmospheric Sciences, 78, 2983–3005, 2021b.

Cooper, W. A., Lasher-Trapp, S. G., and Blyth, A. M.: The Influence of Entrainment and Mixing on the Initial Formation of Rain in a Warm Cumulus Cloud, Journal of the Atmospheric Sciences, 70, 1727 – 1743, https://doi.org/10.1175/JAS-D-12-0128.1, 2013.

Crawford, I., Bower, K. N., Choularton, T. W., Dearden, C., Crosier, J., Westbrook, C., Capes, G., Coe, H., Connolly, P. J., Dorsey, J. R., Gallagher, M. W., Williams, P., Trembath, J., Cui, Z., and Blyth, A.: Ice formation and development in aged, wintertime cumulus over the UK: observations and modelling, Atmos. Chem. Phys., 12, 4963–4985, https://doi.org/10.5194/acp-12-4963-2012, 2012.

Cui, Z., Blyth, A., Huang, Y., Lloyd, G., Choularton, T., Bower, K., Field, P., Hawker, R., and Bennett, L.: Multi-thermals and high concentrations of secondary ice: a modelling study of convective clouds during the Ice in Clouds Experiment – Dust (ICE-D) campaign, Atmospheric Chemistry and Physics, 22, 1649–1667, https://doi.org/10.5194/acp-22-1649-2022, 2022.

Daily, M. I., Robinson, J., Finney, D. L., Raif, E. N., McQuaid, J. B., Sánchez-Marroquín, A., Hu, K., Lloyd, G., Flynn, M., Field, P. R., et al.: Ice-nucleating particle and cloud ice crystal concentrations associated with developing summertime deep convective clouds in south-western USA, Authorea Preprints, 2025.

DeMott, P. J., Prenni, A. J., Liu, X., Kreidenweis, S. M., Petters, M. D., Twohy, C. H., Richardson, M. S., Eidhammer, T., and Rogers, D. C.: Predicting global atmospheric ice nuclei distributions and their impacts on climate, Proc. Natl. Acad. Sci. U.S.A., 107, 11 217–11 222, https://doi.org/10.1073/pnas.0910818107, 2010.

Erfani, E. and Mitchell, D.: A partial mechanistic understanding of the North American monsoon, Journal of Geophysical Research: Atmospheres, 119, 13–096, 2014.

Faber, S., French, J. R., and Jackson, R.: Laboratory and in-flight evaluation of measurement uncertainties from a commercial Cloud Droplet Probe (CDP), Atmospheric Measurement Techniques, 11, 3645–3659, https://doi.org/10.5194/amt-11-3645-2018, 2018.

Field, P. R. and Heymsfield, A. J.: Importance of snow to global precipitation, Geophys. Res. Lett., 42, 9512–9520, https://doi.org/https://doi.org/10.1002/2015GL065497, 2015.

Field, P. R., Lawson, R. P., Brown, P. R. A., Lloyd, G., Westbrook, C., Moisseev, D., Miltenberger, A., Nenes, A., Blyth, A., Choularton, T., Connolly, P., Buehl, J., Crosier, J., Cui, Z., Dearden, C., DeMott, P., Flossmann, A., Heymsfield, A., Huang, Y., Kalesse, H., Kanji, Z. A., Korolev, A., Kirchgaessner, A., Lasher-Trapp, S., Leisner, T., McFarquhar, G., Phillips, V., Stith, J., and Sullivan, S.: Secondary Ice Production: Current State of the Science and Recommendations for the Future, Meteorol. Monogr., 58, 7.1–7.20, https://doi.org/10.1175/AMSMONOGRAPHS-D-16-0014.1, 2017.

Finney, D. L., Blyth, A. M., Gallagher, M., Wu, H., Nott, G. J., Biggerstaff, M. I., Sonnenfeld, R. G., Daily, M., Walker, D., Dufton, D., Bower, K., Böing, S., Choularton, T., Crosier, J., Groves, J., Field, P. R., Coe, H., Murray, B. J., Lloyd, G., Marsden, N. A., Flynn, M., Hu, K., Thamban, N. M., Williams, P. I., Connolly, P. J., McQuaid, J. B., Robinson, J., Cui, Z., Burton, R. R., Carrie, G., Moore, R., Abel, S. J., Tiddeman, D., and Aulich, G.: Deep Convective Microphysics Experiment (DCMEX) coordinated aircraft and ground observations: microphysics, aerosol, and dynamics during cumulonimbus development, Earth System Science Data, 16, 2141–2163, https://doi.org/10.5194/essd-16-2141-2024, 2024.

Fonseca-Hernandez, M., Turrent, C., Mayor, Y. G., and Tereshchenko, I.: Using observational and reanalysis data to explore the southern Gulf of California boundary layer during the North American monsoon onset, Journal of Geophysical Research: Atmospheres, 126, e2020JD033 508, 2021.

Fowler, K., Connolly, P., and Topping, D.: Modelling the effect of condensed-phase diffusion on the homogeneous nucleation of ice in ultra-viscous particles, Atmos. Chem. Phys., 20, 683–698, https://doi.org/10.5194/acp-20-683-2020, 2020.

Grabowski, W. W. and Wang, L.-P.: Growth of Cloud Droplets in a Turbulent Environment, Annu. Rev. Fluid Mech, 45, 293–324, https://doi.org/10.1146/annurev-fluid-011212-140750, 2013.

Grzegorczyk, P., Yadav, S., Zanger, F., Theis, A., Mitra, S. K., Borrmann, S., and Szakáll, M.: Fragmentation of ice particles: laboratory experiments on graupel–graupel and graupel–snowflake collisions, Atmospheric Chemistry and Physics, 23, 13 505–13 521, https://doi.org/10.5194/acp-23-13505-2023, 2023.

Grzegorczyk, P., Wobrock, W., Canzi, A., Niquet, L., Tridon, F., and Planche, C.: Investigating secondary ice production in a deep convective cloud with a 3D bin microphysics model: Part I - Sensitivity study of microphysical processes representations, Atmospheric Research, 313, 107 774, https://doi.org/https://doi.org/10.1016/j.atmosres.2024.107774, 2025.

Hallett, J. and Mossop, S.: Production of secondary ice particles during the riming process, Nature, 249, 26–28, 1974a.

Hallett, J. and Mossop, S. C.: Production of secondary ice particles during the riming process, Nature, 249, 26–28, https://doi.org/10.1038/249026a0, 1974b.

Hallett, J., Sax, R. I., Lamb, D., and Murty, A. R.: Aircraft measurements of ice in Florida cumuli, Quarterly Journal of the Royal Meteorological Society, 104, 631–651, 1978.

Harris-Hobbs, R. L. and Cooper, W. A.: Field evidence supporting quantitative predictions of secondary ice production rates, Journal of Atmospheric Sciences, 44, 1071–1082, 1987.

Huang, Y., Chubb, T., Baumgardner, D., deHoog, M., Siems, S. T., and Manton, M. J.: Evidence for secondary ice production in Southern Ocean open cellular convection, Q. J. R. Meteorol. Soc., 143, 1685–1703, https://doi.org/https://doi.org/10.1002/qj.3041, 2017.

Huang, Y., Wu, W., McFarquhar, G. M., Xue, M., Morrison, H., Milbrandt, J., Korolev, A. V., Hu, Y., Qu, Z., Wolde, M., Nguyen, C., Schwarzenboeck, A., and Heckman, I.: Microphysical processes producing high ice water contents (HIWCs) in tropical convective clouds during the HAIC-HIWC field campaign: dominant role of secondary ice production, Atmos. Chem. Phys., 22, 2365–2384, https://doi.org/10.5194/acp-22-2365-2022, 2022.

Jackson, R. C., McFarquhar, G. M., Stith, J., Beals, M., Shaw, R. A., Jensen, J., Fugal, J., and Korolev, A.: An assessment of the impact of antishattering tips and artifact removal techniques on cloud ice size distributions measured by the 2D cloud probe, Journal of Atmospheric and Oceanic Technology, 31, 2567–2590, 2014.

Jacobson, M. Z.: Fundamentals of atmospheric modeling, Cambridge university press, 1999.

Jacobson, M. Z.: Fundamentals of Atmospheric Modeling, Cambridge University Press, 2 edn., https://doi.org/10.1017/CBO9781139165389, 2005.

James, R. L., Phillips, V. T. J., and Connolly, P. J.: Secondary ice production during the break-up of freezing water drops on impact with ice particles, Atmos. Chem. Phys., 21, 18 519–18 530, https://doi.org/10.5194/acp-21-18519-2021, 2021.

James, R. L., Crosier, J., and Connolly, P. J.: A bin microphysics parcel model investigation of secondary ice formation in an idealised shallow convective cloud, Atmospheric Chemistry and Physics, 23, 9099–9121, https://doi.org/10.5194/acp-23-9099-2023, 2023.

Johnson, M., Xue, M., and Jung, Y.: Comparison of a Spectral Bin and Two Multi-Moment Bulk Microphysics Schemes for Supercell Simulation: Investigation into Key Processes Responsible for Hydrometeor Distributions and Precipitation, Advances in Atmospheric Sciences, 41, 784–800, 2024.

Keinert, A., Spannagel, D., Leisner, T., and Kiselev, A.: Secondary ice production upon freezing of freely falling drizzle droplets, Journal of the Atmospheric Sciences, 77, 2959–2967, 2020.

Koop, T., Luo, B., Tsias, A., and Peter, T.: Water activity as the determinant for homogeneous ice nucleation in aqueous solutions, Nature, 406, 611–614, https://doi.org/10.1038/35020537, 2000.

Korolev, A. and Leisner, T.: Review of experimental studies of secondary ice production, Atmospheric Chemistry and Physics, 20, 11 767–11 797, https://doi.org/10.5194/acp-20-11767-2020, 2020.

Korolev, A., Strapp, J., Isaac, G., and Nevzorov, A.: The Nevzorov airborne hot-wire LWC–TWC probe: Principle of operation and performance characteristics, Journal of Atmospheric and Oceanic Technology, 15, 1495–1510, 1998.

Korolev, A., Emery, E., and Creelman, K.: Modification and tests of particle probe tips to mitigate effects of ice shattering, Journal of Atmospheric and Oceanic Technology, 30, 690–708, 2013.

Korolev, A., Heckman, I., Wolde, M., Ackerman, A. S., Fridlind, A. M., Ladino, L. A., Lawson, R. P., Milbrandt, J., and Williams, E.: A new look at the environmental conditions favorable to secondary ice production, Atmospheric Chemistry and Physics, 20, 1391–1429, https://doi.org/10.5194/acp-20-1391-2020, 2020.

Korolev, A., DeMott, P. J., Heckman, I., Wolde, M., Williams, E., Smalley, D. J., and Donovan, M. F.: Observation of secondary ice production in clouds at low temperatures, Atmospheric Chemistry and Physics, 22, 13 103–13 113, https://doi.org/10.5194/acp-22-13103-2022, 2022.

Ladino, L. A., Korolev, A., Heckman, I., Wolde, M., Fridlind, A. M., and Ackerman, A. S.: On the role of ice-nucleating aerosol in the formation of ice particles in tropical mesoscale convective systems, Geophysical research letters, 44, 1574–1582, 2017.

Lance, S., Brock, C., Rogers, D., and Gordon, J.: Water droplet calibration of the Cloud Droplet Probe (CDP) and in-flight performance in liquid, ice and mixed-phase clouds during ARCPAC, Atmospheric Measurement Techniques, 3, 1683–1706, 2010a.

Lance, S., Brock, C. A., Rogers, D., and Gordon, J. A.: Water droplet calibration of the Cloud Droplet Probe (CDP) and in-flight performance in liquid, ice and mixed-phase clouds during ARCPAC, Atmospheric Measurement Techniques, 3, 1683–1706, https://doi.org/10.5194/amt-3-1683-2010, 2010b.

Lasher-Trapp, S., Cooper, W., and Blyth, A.: Broadening of droplet size distributions from entrainment and mixing in a cumulus cloud, QJ Roy. Meteor. Soc., 131, 195–220, 2005.

Lasher-Trapp, S., Leon, D. C., DeMott, P. J., Villanueva-Birriel, C. M., Johnson, A. V., Moser, D. H., Tully, C. S., and Wu, W.: A multisensor investigation of rime splintering in tropical maritime cumuli, Journal of the Atmospheric Sciences, 73, 2547–2564, 2016.

Lasher-Trapp, S., Scott, E. L., Järvinen, E., Schnaiter, M., Waitz, F., DeMott, P. J., McCluskey, C. S., and Hill, T. C.: Observations and modeling of rime splintering in Southern Ocean cumuli, Journal of Geophysical Research: Atmospheres, 126, e2021JD035 479, 2021.

Lauber, A., Kiselev, A., Pander, T., Handmann, P., and Leisner, T.: Secondary ice formation during freezing of levitated droplets, Journal of the Atmospheric Sciences, 75, 2815–2826, 2018.

Lawson, R. P., Woods, S., and Morrison, H.: The Microphysics of Ice and Precipitation Development in Tropical Cumulus Clouds, J. Atmos. Sci., 72, 2429 – 2445, https://doi.org/10.1175/JAS-D-14-0274.1, 2015.

Lee, H. and Baik, J.-J.: A Comparative Study of Bin and Bulk Cloud Microphysics Schemes in Simulating a Heavy Precipitation Case, Atmosphere, 9, https://doi.org/10.3390/atmos9120475, 2018.

Lehmann, K., Siebert, H., and Shaw, R.: Homogeneous and Inhomogeneous Mixing in Cumulus Clouds: Dependence on Local Turbulence Structure, Journal of The Atmospheric Sciences - J ATMOS SCI, 66, 3641–3659, https://doi.org/10.1175/2009JAS3012.1, 2009.

Leisner, T., Pander, T., Handmann, P., and Kiselev, A.: Secondary ice processes upon heterogeneous freezing of cloud droplets, in: 14th Conf. on Cloud Physics and Atmospheric Radiation, 2014.

Lim, J.-S. and Hoffmann, F.: Life cycle evolution of mixing in shallow cumulus clouds, Journal of Geophysical Research: Atmospheres, 129, e2023JD040 393, 2024.

Lloyd, G., Hu, K., Wu, H., Flynn, M., Bower, K., Marsden, N., Choularton, T., Daily, M., Murray, B., Coe, H., et al.: Overview of Secondary Ice Production In the Deep Convective Microphysics Experiment (DCMEX), 2024.

Lu, C., Liu, Y., Xu, X., Gao, S., and Sun, C.: Entrainment, mixing, and their microphysical influences, Fast Processes in Large-Scale Atmospheric Models: Progress, Challenges, and Opportunities, pp. 87–120, 2023.

McFarquhar, G. M., Baumgardner, D., Bansemer, A., Abel, S. J., Crosier, J., French, J., Rosenberg, P., Korolev, A., Schwarzoenboeck, A., Leroy, D., et al.: Processing of ice cloud in situ data collected by bulk water, scattering, and imaging probes: Fundamentals, uncertainties, and efforts toward consistency, Meteorological Monographs, 58, 11–1, 2017.

Mignani, C., Creamean, J. M., Zimmermann, L., Alewell, C., and Conen, F.: New type of evidence for secondary ice formation at around $-15\,^{\circ}$C in mixed-phase clouds, Atmospheric Chemistry and Physics, 19, 877–886, https://doi.org/10.5194/acp-19-877-2019, 2019.

Morrison, H., Lawson, P., and Chandrakar, K. K.: Observed and Bin Model Simulated Evolution of Drop Size Distributions in High-Based Cumulus Congestus Over the United Arab Emirates, J. Geophys. Res.: Atmos., 127, e2021JD035 711, https://doi.org/https://doi.org/10.1029/2021JD035711, e2021JD035711 2021JD035711, 2022a.

Morrison, H., Peters, J. M., Chandrakar, K. K., and Sherwood, S. C.: Influences of environmental relative humidity and horizontal scale of subcloud ascent on deep convective initiation, Journal of the Atmospheric Sciences, 79, 337–359, 2022b.

Mossop, S.: Some factors governing ice particle multiplication in cumulus clouds, Journal of Atmospheric Sciences, 35, 2033–2037, 1978.

Petters, M. D. and Kreidenweis, S. M.: A single parameter representation of hygroscopic growth and cloud condensation nucleus activity, Atmos. Chem. Phys., 7, 1961–1971, https://doi.org/10.5194/acp-7-1961-2007, 2007.

Phillips, V. T., Patade, S., Gutierrez, J., and Bansemer, A.: Secondary Ice Production by Fragmentation of Freezing Drops: Formulation and Theory, J. Atmos. Sci., 76, 3031–3070, https://doi.org/10.1175/JAS-D-17-0190.1, 2018a.

Phillips, V. T., Patade, S., Gutierrez, J., and Bansemer, A.: Secondary ice production by fragmentation of freezing drops: Formulation and theory, Journal of the Atmospheric Sciences, 75, 3031–3070, 2018b.

Phillips, V. T. J., Yano, J.-I., and Khain, A.: Ice Multiplication by Breakup in Ice–Ice Collisions. Part I: Theoretical Formulation, J. Atmos. Sci., 74, 1705 – 1719, https://doi.org/10.1175/JAS-D-16-0224.1, 2017.

Planche, C., Wobrock, W., and Flossmann, A. I.: The continuous melting process in a cloud-scale model using a bin microphysics scheme, Quarterly Journal of the Royal Meteorological Society, 140, 1986–1996, 2014.

Pruppacher, H. R. and Klett, J. D.: Microphysics of clouds and precipitation, "Norwell", 1997.

Pruppacher, H. R., Klett, J. D., and Wang, P. K.: Microphysics of clouds and precipitation, 1998.

Qu, Y., Khain, A., Phillips, V., Ilotoviz, E., Shpund, J., Patade, S., and Chen, B.: The Role of Ice Splintering on Microphysics of Deep Convective Clouds Forming Under Different Aerosol Conditions: Simulations Using the Model With Spectral Bin Microphysics, J. Geophys. Res.: Atmos., 125, e2019JD031 312, https://doi.org/https://doi.org/10.1029/2019JD031312, e2019JD031312 2019JD031312, 2020.

Qu, Z., Korolev, A., Milbrandt, J. A., Heckman, I., Huang, Y., McFarquhar, G. M., Morrison, H., Wolde, M., and Nguyen, C.: The impacts of secondary ice production on microphysics and dynamics in tropical convection, Atmospheric Chemistry and Physics, 22, 12 287–12 310, https://doi.org/10.5194/acp-22-12287-2022, 2022.

Rangno, A. L. and Hobbs, P. V.: Ice particle concentrations and precipitation development in small polar maritime cumuliform clouds., Q. J. R. Meteorol. Soc., 117, 207–241, 1991.

Reisner, J., Rasmussen, R. M., and Bruintjes, R. T.: Explicit forecasting of supercooled liquid water in winter storms using the MM5 mesoscale model, Q. J. R. Meteorol. Soc., 124, 1071–1107, https://doi.org/https://doi.org/10.1002/qj.49712454804, 1998.

Schwarzenboeck, A., Shcherbakov, V., Lefevre, R., Gayet, J.-F., Pointin, Y., and Duroure, C.: Indications for stellar-crystal fragmentation in Arctic clouds, Atmospheric Research, 92, 220–228, https://doi.org/https://doi.org/10.1016/j.atmosres.2008.10.002, 2009.

Seidel, J. S., Kiselev, A. A., Keinert, A., Stratmann, F., Leisner, T., and Hartmann, S.: Secondary ice production – no evidence of efficient rime-splintering mechanism, Atmospheric Chemistry and Physics, 24, 5247–5263, https://doi.org/10.5194/acp-24-5247-2024, 2024.

Sotiropoulou, G., Sullivan, S., Savre, J., Lloyd, G., Lachlan-Cope, T., Ekman, A. M. L., and Nenes, A.: The impact of secondary ice production on Arctic stratocumulus, Atmos. Chem. Phys., 20, 1301–1316, https://doi.org/10.5194/acp-20-1301-2020, 2020.

Takahashi, T. and Nagao, Y.: Possible high ice particle production during Graupel-Graupel collisions., Journal of the atmospheric sciences, 52, 1995.

Tan, I., Zhou, C., Lamy, A., and Stauffer, C. L.: Moderate climate sensitivity due to opposing mixed-phase cloud feedbacks, Npj Climate and Atmospheric Science, 8, 86, 2025.

Topping, D. O., Connolly, P. J., and McFiggans, G. B.: Cloud droplet number enhanced by co-condensation of organic vapours, Nature Geoscience, 6, 443–446, https://doi.org/10.1038/ngeo1809, 2013.

Vardiman, L.: The generation of secondary ice particles in clouds by crystal–crystal collision, Journal of Atmospheric Sciences, 35, 2168–2180, 1978.

Wu, H., Marsden, N., Connolly, P., Flynn, M., Williams, P. I., Finney, D., Hu, K., Nott, G. J., Thamban, N., Bower, K., Blyth, A., Gallagher, M., and Coe, H.: The role of aerosols and meteorological conditions in shaping cloud droplet development in New Mexico summer deep-convective systems, EGUsphere, 2025, 1–31, https://doi.org/10.5194/egusphere-2025-2600, 2025a.

Wu, H., Marsden, N., Connolly, P., Flynn, M., Williams, P. I., Finney, D., Hu, K., Nott, G. J., Thamban, N. M., Bower, K., Blyth, A., Gallagher, M., and Coe, H.: The role of aerosols and meteorological conditions in shaping cloud droplet development in New Mexico summer deep-convective systems, Atmospheric Chemistry and Physics, 25, 18 409–18 429, https://doi.org/10.5194/acp-25-18409-2025, 2025b.

Xu, X., Lu, C., Liu, Y., Luo, S., Zhou, X., Endo, S., Zhu, L., and Wang, Y.: Influences of entrainment-mixing parameterization on numerical simulations of cumulus and stratocumulus clouds, Atmospheric Chemistry and Physics Discussions, 2021, 1–40, 2021.

Xu, X., Lu, C., Liu, Y., Luo, S., Zhou, X., Endo, S., Zhu, L., and Wang, Y.: Influences of an entrainment–mixing parameterization on numerical simulations of cumulus and stratocumulus clouds, Atmospheric Chemistry and Physics, 22, 5459–5475, https://doi.org/10.5194/acp-22-5459-2022, 2022.

Yeom, J. M., Yum, S. S., Liu, Y., and Lu, C.: A study on the entrainment and mixing process in the continental stratocumulus clouds measured during the RACORO campaign, Atmospheric research, 194, 89–99, 2017.

Zhao, X. and Liu, X.: Primary and secondary ice production: interactions and their relative importance, Atmos. Chem. Phys., 22, 2585–2600, https://doi.org/10.5194/acp-22-2585-2022, 2022.